A. Gorgeri, R. Vescovini, L. Dozio
Analysis of Multiple-Core Sandwich Cylindrical Shells Using a Sublaminate Formulation
Composite Structures, Vol. 225, 2019, 111067 (16 pages)
doi:10.1016/j.compstruct.2019.111067

Analysis of Multiple-Core Sandwich Cylindrical Shells Using a Sublaminate Formulation

A. Gorgeri, R. Vescovini* and L. Dozio

Dipartimento di Scienze e Tecnologie Aerospaziali, Politecnico di Milano

Via La Masa 34, 20156 Milano, Italy

Abstract

An advanced modelling approach is presented for the linear analysis of multilayered cylindrical shells. It relies on the combined use of a sublaminate shell formulation along with the method of Ritz. The approach is particularly suitable for the analysis of sandwich shells, and can be naturally applied for studying non-conventional configurations characterized by the presence of multiple cores. The formulation relies upon a displacement-based approach and makes it possible the analysis of thin and thick configurations, without restrictions regarding the shallowness of the shell. The quality of the predictions is assessed by comparison against 3D solutions, and the advantages offered by current modeling approach are highlighted in terms of required theory-related degrees of freedom. The flexibility of the formulation is exploited to illustrate the analysis of a triple-core sandwich panel, giving evidence of the advantages offered by the proposed approach for modeling shells characterized by an arbitrary degree of complexity. Novel results are presented for future benchmarking purposes.

Keywords: sandwich; multiple-core; shells; sublaminate; unified formulation; Ritz method.

1 Introduction

Sandwich structures are widely employed both as structural and non-structural members of aerospace constructions. Few but examples are aircraft fuselage panels [1, 2], space launcher and rocket shells [3], rotor blades [4] and solar arrays in space satellite [5]. Worth of mention is the use of sandwich panels as a valuable mean for improving acoustic and vibro-acoustic response, which can be particularly relevant for airplane and helicopter cabins [6, 7].

From the aforementioned applications one can note that often the geometry is inherently non-flat, and solutions procedures for plate-like structures cannot be used unless the radii of curvature are very large in

---

*Corresponding author. *Email address:* `riccardo.vescovini@polimi.it` (Riccardo Vescovini) comparison to the typical panel dimensions. For this reason, the analysis of many typical configurations demands for the availability of numerical tools capable of accounting for curved geometries and highly hetereogeneous thickness-wise behaviour.

A vast literature exists on modeling and analysis of composite shell, an excellent review of which is available in Refs. [8–11]. In this context, a common classification [10] refers to thin (see, e.g., [12]), high-order [13–16] and layer-wise [13, 17–21] shell theories. The first class, which includes well-known theories due to Donnell, Flügge and Sanders, offers the advantage of keeping the number of theory-related degrees of freedom low. This feature can be exploited to derive simple analytical solutions or efficient semi-analytical approaches, see e.g. [22–25]. However, their applicability is limited to the prediction of the gross behaviour of thin shells [26], and local response, as well as the effects of shear deformability, are not accurately captured. In the case of sandwich panels the above issues are even amplified. On the contrary, detailed predictions and failure characteristics of composite shells can be achieved by retaining the effects of normal and transverse shear deformability, whose importance is a well-known aspect. To this aim, several efforts were directed towards the development of theories for thick composite shells in the last decades. In this context, it is worth mentioning the variable-kinematic approach proposed by Carrera [27, 28], commonly referred to as CUF, which is capable of embedding equivalent single layer (ESL) and layer-wise (LW) theories in a compact and unified way. Applications to shell problems are well documented for mechanical [29–31], thermo-elastic [32] and electro-mechanical [33] analyses. When dealing with monolithic shells, a uniform kinematic description – i.e. same theory irrespective on the ply or group of plies – appears to be the most logical approach. However, when it turns to the case of sandwich shells, the inherent thickness-wise heterogeneity suggests the adoption of theories characterized by different levels of refinement depending on the thickness-wise position, distinguishing between layers belonging to the skins and the core at least. In this sense, a unique axiomatic description of the displacement field is very likely to determine a large number of theory-related degrees of freedom, and the adoption of a purely ESL or LW can be suboptimal. To this aim, a sublaminate strategy was proposed by D'Ottavio [34], the main idea consisting in dividing the stack into a number of sublaminates (S), each characterized by an independent kinematic theory. The so-called S-GUF formulation merges the idealization of the stack into sublaminates with the Generalized Unified Formulation (GUF) proposed by Demasi [35]. As a consequence, the so-obtained models are not subjected to any a priori combination of kinematic theories, as it is done in the context of classical sandwich theories [36, 37]. It follows that the ratio between accuracy and number of degrees of freedom can be arbitrarily tuned and maximized depending on the problem at hand.

Past efforts by the authors have dealt with the analysis of flat plates, and bending [38], buckling [39] and thermal buckling [40] were investigated, demonstrating the potentialities offered by the combined use of the S-GUF formulation and the method of Ritz.

As it turns out, no previous attempts can be found regarding the application of the mentioned S-GUF approach to the case of composite and sandwich shells. The present work aims at filling this gap, and illustrates the extension of the S-GUF formulation to cylindrically curved shells.

The theoretical aspects are covered in Section 1, while the capability of the proposed formulation is demonstrated by illustrating the comparison against reference 3D solutions in Section 2.1. Novel results are discussed in Section 2.2, where the versatility of the proposed approach is exploited to assess the free vibration and bending response of a triple-core configuration investigated in a past European Garteur project [7, 41] for the application to helicopter trim panels.

2 Theoretical framework

A cylindrical sandwich shell is considered, as sketched in Fig. 1. A coordinate system (x, y, z) is introduced, where $x \in [0, a]$ and $y \in [0, b]$ span the shell mid-surface and $z \in [-h/2, h/2]$ runs along the thickness-wise direction. The panel has length a, height h and width $b = R\varphi$, where R is the curvature radius of the mid-surface, and φ is the angular width.

Highlighted in the sketch is the discretization of the thickness domain into $k = 1, \ldots, N_k$ sublaminates, each comprising one or more adjacent plies numbered locally from $p = 1$ to $p = N_p^k$. An advanced kinematic modelling scheme, referred to as Sublaminate Generalized Unified Formulation (S-GUF), is adopted that allows for a variable-kinematics, sublaminate-specific description of the structure, as explained later.

According to the notation adopted hereinafter, kinematic quantities and material properties referred to the p-th ply of the k-th sublaminate are indicated as $()^{p,k}$. Local thickness coordinates are introduced as $z_p \in [-h_p/2, h_p/2]$ and $z_k \in [-h_k/2, h_k/2]$, where h_p (h_k) is the thickness of the p-th ply (k-th sublaminate). Non-dimensional coordinates are also introduced as:

$$\zeta_p = \frac{z_p}{h_p/2} \qquad \zeta_k = \frac{z_k}{h_k/2} \tag{1}$$

2.1 Strain-displacement equations and Hooke's law

Within the linear framework, strains and displacements are related by a linear differential operator as:

$$\boldsymbol{\varepsilon}^{p,k} = \mathbf{D}\mathbf{u}^{p,k} \tag{2}$$

where $\mathbf{u}^{p,k} = \left\{ u_x^{p,k} \; u_y^{p,k} \; u_z^{p,k} \right\}^{\mathrm{T}}$ and $\boldsymbol{\varepsilon}^{p,k}$ are the vectors collecting the displacement and strain components, respectively, while $\mathbf{D}$ is the differential operator whose expression depends upon the panel geometry [13]. The gradient equations are applied here to the case of circular cylindrical shells, for which the following relations hold:

$$\varepsilon_x^{p,k} = \frac{\partial u_x^{p,k}}{\partial x}$$

$$
\begin{aligned}
\varepsilon_y^{p,k} &= \frac{1}{1+z/R}\left(\frac{\partial u_y^{p,k}}{\partial y} + \frac{u_z^{p,k}}{R}\right) \\
\gamma_{xy}^{p,k} &= \frac{\partial u_y^{p,k}}{\partial x} + \frac{1}{1+z/R}\frac{\partial u_x^{p,k}}{\partial y} \\
\gamma_{yz}^{p,k} &= \frac{\partial u_y^{p,k}}{\partial z} + \frac{1}{1+z/R}\left(\frac{\partial u_z^{p,k}}{\partial y} - \frac{u_y^{p,k}}{R}\right) \\
\gamma_{xz}^{p,k} &= \frac{\partial u_x^{p,k}}{\partial z} + \frac{\partial u_z^{p,k}}{\partial x} \\
\varepsilon_z^{p,k} &= \frac{\partial u_z^{p,k}}{\partial z}
\end{aligned}
\tag{3}
$$

Note that the relations given by Eq. (3) are derived by introducing the assumption of infinitesimal displacements, whilst no further simplifications are made regarding the shell shallowness. It follows that the formulation is developed to analyze both shallow and deep shells.

A compact vector notation is introduced as follows:

$$\boldsymbol{\varepsilon}_\Omega^{p,k} = \left(\mathbf{D}_\Omega + \mathbf{A}_\Omega\right)\mathbf{u}^{p,k} \tag{4}$$

and:

$$\boldsymbol{\varepsilon}_\mathrm{n}^{p,k} = \left(\mathbf{D}_\mathrm{n} - \mathbf{A}_\mathrm{n} + \mathbf{D}_\mathrm{z}\right)\mathbf{u}^{p,k} \tag{5}$$

where the in-plane and out-of-plane strain components are organized as:

$$\boldsymbol{\varepsilon}_\Omega = \left\{ \begin{array}{ccc} \varepsilon_x & \varepsilon_y & \gamma_{xy} \end{array} \right\}^\mathrm{T} \qquad \boldsymbol{\varepsilon}_\mathrm{n} = \left\{ \begin{array}{ccc} \gamma_{yz} & \gamma_{xz} & \varepsilon_z \end{array} \right\}^\mathrm{T} \tag{6}$$

and:

$$\mathbf{D}_\Omega = \begin{bmatrix} \frac{\partial}{\partial x} & 0 & 0 \\ 0 & \frac{1}{B}\frac{\partial}{\partial y} & 0 \\ \frac{1}{B}\frac{\partial}{\partial y} & \frac{\partial}{\partial x} & 0 \end{bmatrix} \qquad \mathbf{A}_\Omega = \begin{bmatrix} 0 & 0 & 0 \\ 0 & 0 & \frac{1}{B}\frac{1}{R} \\ 0 & 0 & 0 \end{bmatrix} \tag{7}$$

$$\mathbf{D}_\mathrm{n} = \begin{bmatrix} 0 & 0 & \frac{1}{B}\frac{\partial}{\partial y} \\ 0 & 0 & \frac{\partial}{\partial x} \\ 0 & 0 & 0 \end{bmatrix} \qquad \mathbf{A}_\mathrm{n} = \begin{bmatrix} 0 & \frac{1}{B}\frac{1}{R} & 0 \\ 0 & 0 & 0 \\ 0 & 0 & 0 \end{bmatrix} \qquad \mathbf{D}_\mathrm{z} = \begin{bmatrix} 0 & \frac{\partial}{\partial z} & 0 \\ \frac{\partial}{\partial z} & 0 & 0 \\ 0 & 0 & \frac{\partial}{\partial z} \end{bmatrix} \tag{8}$$

where $B = 1 + z/R$ is the Lamé coefficient along the y direction.

It is worth noting that $\mathbf{D}_\mathrm{z}$ is the same as in the case of flat plates, while $\mathbf{D}_\Omega$ and $\mathbf{D}_\mathrm{n}$ depend on the variation of the local curvature radius with respect to the z-coordinate. In addition, $\mathbf{A}_\Omega$ accounts for the hoop strain due to radial displacements, while $\mathbf{A}_\mathrm{n}$accounts for the transverse shear deformation due to circumferential displacements.

Within the framework of linear elasticity, the Hooke's law for orthotropic materials reads:

$$
\begin{aligned}
\boldsymbol{\sigma}_\Omega^{p,k} &= \tilde{\mathbf{C}}_{\Omega\Omega}^{p,k}\boldsymbol{\varepsilon}_\Omega^{p,k} + \tilde{\mathbf{C}}_{\Omega\mathrm{n}}^{p,k}\boldsymbol{\varepsilon}_\mathrm{n}^{p,k} \\
\boldsymbol{\sigma}_\mathrm{n}^{p,k} &= \tilde{\mathbf{C}}_{\mathrm{n}\Omega}^{p,k}\boldsymbol{\varepsilon}_\Omega^{p,k} + \tilde{\mathbf{C}}_{\mathrm{nn}}^{p,k}\boldsymbol{\varepsilon}_\mathrm{n}^{p,k}
\end{aligned}
\tag{9}
$$

where:

$$\boldsymbol{\sigma}_{\Omega}^{p,k} = \left\{ \begin{array}{ccc} \sigma_x^{p,k} & \sigma_y^{p,k} & \tau_{xy}^{p,k} \end{array} \right\}^{\mathrm{T}} \qquad \boldsymbol{\sigma}_{\mathrm{n}}^{p,k} = \left\{ \begin{array}{ccc} \tau_{yz}^{p,k} & \tau_{xz}^{p,k} & \sigma_z^{p,k} \end{array} \right\}^{\mathrm{T}} \tag{10}$$

and:

$$\begin{aligned} \tilde{\mathbf{C}}_{\Omega\Omega}^{p,k} &= \begin{bmatrix} \tilde{C}_{11}^{p,k} & \tilde{C}_{12}^{p,k} & \tilde{C}_{16}^{p,k} \\ \tilde{C}_{12}^{p,k} & \tilde{C}_{22}^{p,k} & \tilde{C}_{26}^{p,k} \\ \tilde{C}_{16}^{p,k} & \tilde{C}_{26}^{p,k} & \tilde{C}_{66}^{p,k} \end{bmatrix} & \tilde{\mathbf{C}}_{\Omega\mathrm{n}}^{p,k} &= \begin{bmatrix} 0 & 0 & \tilde{C}_{13}^{p,k} \\ 0 & 0 & \tilde{C}_{23}^{p,k} \\ 0 & 0 & \tilde{C}_{36}^{p,k} \end{bmatrix} \\ \tilde{\mathbf{C}}_{\mathrm{n}\Omega}^{p,k} &= \begin{bmatrix} 0 & 0 & 0 \\ 0 & 0 & 0 \\ \tilde{C}_{13}^{p,k} & \tilde{C}_{23}^{p,k} & \tilde{C}_{36}^{p,k} \end{bmatrix} & \tilde{\mathbf{C}}_{\mathrm{nn}}^{p,k} &= \begin{bmatrix} \tilde{C}_{44}^{p,k} & \tilde{C}_{45}^{p,k} & 0 \\ \tilde{C}_{45}^{p,k} & \tilde{C}_{55}^{p,k} & 0 \\ 0 & 0 & \tilde{C}_{33}^{p,k} \end{bmatrix} \end{aligned} \tag{11}$$

2.2 The Hamilton's principle using S-GUF description

The governing equations are derived according to the general form of the Hamilton's principle [42], that is written as:

$$\int_{t_1}^{t_2} \big[\delta K - (\delta U + \delta V)\big] \; \mathrm{d}t = 0 \tag{12}$$

where the virtual variation of strain energy is:

$$\delta U \equiv \delta W_i = \int_V \delta\boldsymbol{\varepsilon}^{\mathrm{T}}\boldsymbol{\sigma} \, \mathrm{d}V \tag{13}$$

and the virtual variation of potential energy due to the a set of normal pressure loads applied at the top (f_z^{top}) and bottom (f_z^{bot}) faces of the laminate reads:

$$\delta V \equiv -\delta W_e^p = -\int_{\Omega_{\mathrm{top}}} \delta u_{\mathrm{top}} f_z^{\mathrm{top}} \, \mathrm{d}\Omega_{\mathrm{top}} - \int_{\Omega_{\mathrm{bot}}} \delta u_{\mathrm{bot}} f_z^{\mathrm{bot}} \, \mathrm{d}\Omega_{\mathrm{bot}} \tag{14}$$

where δW_e^p is the external virtual work, and $u_{\mathrm{bot/top}} = u_z(x, y, \pm h/2)$ are the z-components of the displacement field evaluated at the inner and outer surfaces Ω_{top} and Ω_{bot}, respectively.
The virtual variation of kinetic energy is:

$$\delta K = \int_V \delta\dot{\mathbf{u}}^{\mathrm{T}} \rho \, \dot{\mathbf{u}} \, \mathrm{d}V \tag{15}$$

where the dot denotes the time derivative. The expression of Eq. (15) can be integrated by part, leading to:

$$\int_{t_1}^{t_2} \delta\dot{\mathbf{u}}^{\mathrm{T}} \rho \, \dot{\mathbf{u}} \, \mathrm{d}t = \delta\mathbf{u}^{\mathrm{T}} \rho \, \dot{\mathbf{u}}\Big|_{t_1}^{t_2} - \int_{t_1}^{t_2} \delta\mathbf{u}^{\mathrm{T}} \rho \, \ddot{\mathbf{u}} \, \mathrm{d}t \tag{16}$$

where the double dot denotes the second time derivative. Noting that $\delta\mathbf{u}(t_1) = \delta\mathbf{u}(t_2) = 0$, the virtual variation of the kinetic energy can be rewritten as:

$$\delta K \equiv \delta W_e^i = -\int_V \delta\mathbf{u}^{\mathrm{T}} \rho \, \ddot{\mathbf{u}} \, \mathrm{d}V \tag{17}$$

As seen form Eq. (17), the variational statement obtained by means of the Hamilton's principle is equivalent to the Principle of Virtual Displacements (PVD) applied to dynamical systems, provided the accelerations are considered as external forces, according to the D'Alembert principle. Accordingly, the present formulation, when referred to the static case, can be seen as an application of the PVD.
The infinitesimal volume element in the chosen reference frame is:

$$\mathrm{d}V = \left(1+\frac{z}{R}\right)\,\mathrm{d}x\,\mathrm{d}y\,\mathrm{d}z = \left(1+\frac{z}{R}\right)\,\mathrm{d}\Omega\,\mathrm{d}z \tag{18}$$

The internal virtual work, accounting for the S-GUF subdivision of the stack into sublaminates and making use of Eq. (18), reads:

$$\delta W_i = \int_\Omega\int_{-h/2}^{h/2}\delta\boldsymbol{\varepsilon}^{\mathrm{T}}\boldsymbol{\sigma}\left(1+\frac{z}{R}\right)\mathrm{d}z\,\mathrm{d}\Omega = \sum_{k=1}^{N_k}\sum_{p=1}^{N_p^k}\int_\Omega\int_{z_p^{\mathrm{bot}}}^{z_p^{\mathrm{top}}}\left(\delta\boldsymbol{\varepsilon}_\Omega^{p,k^{\mathrm{T}}}\boldsymbol{\sigma}_\Omega^{p,k}+\delta\boldsymbol{\varepsilon}_{\mathrm{n}}^{p,k^{\mathrm{T}}}\boldsymbol{\sigma}_{\mathrm{n}}^{p,k}\right)\left(1+\frac{z_p}{R}\right)\mathrm{d}z_p\,\mathrm{d}\Omega \tag{19}$$

Similarly, the external virtual works become, respectively:

$$\delta W_e^i = -\int_\Omega\int_{-h/2}^{h/2}\delta\mathbf{u}^{\mathrm{T}}\rho\,\ddot{\mathbf{u}}\left(1+\frac{z}{R}\right)\mathrm{d}z\,\mathrm{d}\Omega = -\sum_{k=1}^{N_k}\sum_{p=1}^{N_p^k}\int_\Omega\int_{z_p^{\mathrm{bot}}}^{z_p^{\mathrm{top}}}\delta\mathbf{u}^{p,k^{\mathrm{T}}}\rho^{p,k}\,\ddot{\mathbf{u}}^{p,k}\left(1+\frac{z_p}{R}\right)\mathrm{d}z_p\,\mathrm{d}\Omega \tag{20}$$

$$\delta W_e^p = \int_\Omega \delta u_{\mathrm{top}}^{N_p^k,N_k}f_z^{\mathrm{top}}\left(1+\frac{h}{2R}\right)\mathrm{d}\Omega + \int_\Omega \delta u_{\mathrm{bot}}^{1,1}f_z^{\mathrm{bot}}\left(1-\frac{h}{2R}\right)\mathrm{d}\Omega \tag{21}$$

Substituting Eqs. (3) and (9) into Eq. (19), the two contributions of the internal virtual work are expressed as functions of the displacement variables as:

$$\begin{aligned}
\delta\boldsymbol{\varepsilon}_\Omega^{p,k^{\mathrm{T}}}\boldsymbol{\sigma}_\Omega^{p,k} &= \delta\boldsymbol{\varepsilon}_\Omega^{p,k^{\mathrm{T}}}(\tilde{\mathbf{C}}_{\Omega\Omega}^{p,k}\boldsymbol{\epsilon}_\Omega^{p,k}+\tilde{\mathbf{C}}_{\Omega\mathrm{n}}^{p,k}\boldsymbol{\epsilon}_{\mathrm{n}}^{p,k}) = \\
&= \delta(\mathbf{D}_\Omega\mathbf{u}^{p,k})^{\mathrm{T}}\tilde{\mathbf{C}}_{\Omega\Omega}^{p,k}\mathbf{D}_\Omega\mathbf{u}^{p,k}+\delta(\mathbf{D}_\Omega\mathbf{u}^{p,k})^{\mathrm{T}}\tilde{\mathbf{C}}_{\Omega\Omega}^{p,k}\mathbf{A}_\Omega\mathbf{u}^{p,k}+ \\
&\quad+\delta(\mathbf{D}_\Omega\mathbf{u}^{p,k})^{\mathrm{T}}\tilde{\mathbf{C}}_{\Omega\mathrm{n}}^{p,k}\mathbf{D}_{\mathrm{n}}\mathbf{u}^{p,k}-\delta(\mathbf{D}_\Omega\mathbf{u}^{p,k})^{\mathrm{T}}\tilde{\mathbf{C}}_{\Omega\mathrm{n}}^{p,k}\mathbf{A}_{\mathrm{n}}\mathbf{u}^{p,k}+\delta(\mathbf{D}_\Omega\mathbf{u}^{p,k})^{\mathrm{T}}\tilde{\mathbf{C}}_{\Omega\mathrm{n}}^{p,k}\mathbf{D}_z\mathbf{u}^{p,k}+ \\
&\quad+\delta(\mathbf{A}_\Omega\mathbf{u}^{p,k})^{\mathrm{T}}\tilde{\mathbf{C}}_{\Omega\Omega}^{p,k}\mathbf{D}_\Omega\mathbf{u}^{p,k}+\delta(\mathbf{A}_\Omega\mathbf{u}^{p,k})^{\mathrm{T}}\tilde{\mathbf{C}}_{\Omega\Omega}^{p,k}\mathbf{A}_\Omega\mathbf{u}^{p,k}+ \\
&\quad+\delta(\mathbf{A}_\Omega\mathbf{u}^{p,k})^{\mathrm{T}}\tilde{\mathbf{C}}_{\Omega\mathrm{n}}^{p,k}\mathbf{D}_{\mathrm{n}}\mathbf{u}^{p,k}-\delta(\mathbf{A}_\Omega\mathbf{u}^{p,k})^{\mathrm{T}}\tilde{\mathbf{C}}_{\Omega\mathrm{n}}^{p,k}\mathbf{A}_{\mathrm{n}}\mathbf{u}^{p,k}+\delta(\mathbf{A}_\Omega\mathbf{u}^{p,k})^{\mathrm{T}}\tilde{\mathbf{C}}_{\Omega\mathrm{n}}^{p,k}\mathbf{D}_z\mathbf{u}^{p,k}
\end{aligned} \tag{22}$$

$$\begin{aligned}
\delta\boldsymbol{\varepsilon}_{\mathrm{n}}^{p,k^{\mathrm{T}}}\boldsymbol{\sigma}_{\mathrm{n}}^{p,k} &= \delta\boldsymbol{\varepsilon}_{\mathrm{n}}^{p,k^{\mathrm{T}}}(\tilde{\mathbf{C}}_{\mathrm{n}\Omega}^{p,k}\boldsymbol{\epsilon}_\Omega^{p,k}+\tilde{\mathbf{C}}_{\mathrm{nn}}^{p,k}\boldsymbol{\epsilon}_{\mathrm{n}}^{p,k}) = \\
&= \delta(\mathbf{D}_{\mathrm{n}}\mathbf{u}^{p,k})^{\mathrm{T}}\tilde{\mathbf{C}}_{\mathrm{n}\Omega}^{p,k}\mathbf{D}_\Omega\mathbf{u}^{p,k}+\delta(\mathbf{D}_{\mathrm{n}}\mathbf{u}^{p,k})^{\mathrm{T}}\tilde{\mathbf{C}}_{\mathrm{n}\Omega}^{p,k}\mathbf{A}_\Omega\mathbf{u}^{p,k}+ \\
&\quad+\delta(\mathbf{D}_{\mathrm{n}}\mathbf{u}^{p,k})^{\mathrm{T}}\tilde{\mathbf{C}}_{\mathrm{nn}}^{p,k}\mathbf{D}_{\mathrm{n}}\mathbf{u}^{p,k}-\delta(\mathbf{D}_{\mathrm{n}}\mathbf{u}^{p,k})^{\mathrm{T}}\tilde{\mathbf{C}}_{\mathrm{nn}}^{p,k}\mathbf{A}_{\mathrm{n}}\mathbf{u}^{p,k}+\delta(\mathbf{D}_{\mathrm{n}}\mathbf{u}^{p,k})^{\mathrm{T}}\tilde{\mathbf{C}}_{\mathrm{nn}}^{p,k}\mathbf{D}_z\mathbf{u}^{p,k}+ \\
&\quad-\delta(\mathbf{A}_{\mathrm{n}}\mathbf{u}^{p,k})^{\mathrm{T}}\tilde{\mathbf{C}}_{\mathrm{n}\Omega}^{p,k}\mathbf{D}_\Omega\mathbf{u}^{p,k}-\delta(\mathbf{A}_{\mathrm{n}}\mathbf{u}^{p,k})^{\mathrm{T}}\tilde{\mathbf{C}}_{\mathrm{n}\Omega}^{p,k}\mathbf{A}_\Omega\mathbf{u}^{p,k}+ \\
&\quad-\delta(\mathbf{A}_{\mathrm{n}}\mathbf{u}^{p,k})^{\mathrm{T}}\tilde{\mathbf{C}}_{\mathrm{nn}}^{p,k}\mathbf{D}_{\mathrm{n}}\mathbf{u}^{p,k}+\delta(\mathbf{A}_{\mathrm{n}}\mathbf{u}^{p,k})^{\mathrm{T}}\tilde{\mathbf{C}}_{\mathrm{nn}}^{p,k}\mathbf{A}_{\mathrm{n}}\mathbf{u}^{p,k}-\delta(\mathbf{A}_{\mathrm{n}}\mathbf{u}^{p,k})^{\mathrm{T}}\tilde{\mathbf{C}}_{\mathrm{nn}}^{p,k}\mathbf{D}_z\mathbf{u}^{p,k}+ \\
&\quad+\delta(\mathbf{D}_{\mathrm{z}}\mathbf{u}^{p,k})^{\mathrm{T}}\tilde{\mathbf{C}}_{\mathrm{n}\Omega}^{p,k}\mathbf{D}_\Omega\mathbf{u}^{p,k}+\delta(\mathbf{D}_{\mathrm{z}}\mathbf{u}^{p,k})^{\mathrm{T}}\tilde{\mathbf{C}}_{\mathrm{n}\Omega}^{p,k}\mathbf{A}_\Omega\mathbf{u}^{p,k}+ \\
&\quad+\delta(\mathbf{D}_{\mathrm{z}}\mathbf{u}^{p,k})^{\mathrm{T}}\tilde{\mathbf{C}}_{\mathrm{nn}}^{p,k}\mathbf{D}_{\mathrm{n}}\mathbf{u}^{p,k}-\delta(\mathbf{D}_{\mathrm{z}}\mathbf{u}^{p,k})^{\mathrm{T}}\tilde{\mathbf{C}}_{\mathrm{nn}}^{p,k}\mathbf{A}_{\mathrm{n}}\mathbf{u}^{p,k}+\delta(\mathbf{D}_{\mathrm{z}}\mathbf{u}^{p,k})^{\mathrm{T}}\tilde{\mathbf{C}}_{\mathrm{nn}}^{p,k}\mathbf{D}_z\mathbf{u}^{p,k}
\end{aligned} \tag{23}$$

Combining Eqs. (19)-(23) according to Eq. (12), the equilibrium conditions expressed by the PVD are formulated as functions of the unknown components of the displacement field, therefore a fully displacement-based variational statement of general validity is obtained.

The problem is specialized to a 2D formulation by introducing the thickness-wise approximation of the displacement field based on the S-GUF approach. In particular, the thickness domain is formally divided into sublaminates to collect one or more adjacent plies; each sublaminate is described by a proper kinematic theory, either Equivalent Single Layer (ESL) where a common set of kinematic variables is shared by all the plies within the sublaminate, or Layer-Wise (LW) where ply-specific kinematic variables are employed. These features render the proposed formulation particularly suited for sandwich panels, typically characterized by drastic heterogeneity along the thickness direction. The sublaminate description allows to catch the slope discontinuities of the displacement field, and to make use of high-order theories just where they are needed, therefore minimizing the number of theory-related degrees of freedom (DOFs) and, in turn, the computational cost.

The displacement field associated with the generic ply p of the sublaminate k is postulated as:

$$\begin{cases} u_x^{p,k}(x,y,z_p,t) = F_{\beta_{u_x}}(z_p)u_{x\beta_{u_x}}^{p,k}(x,y,t) & \beta_{u_x} = 0,1,\dots,N_{u_x}^k \\ u_y^{p,k}(x,y,z_p,t) = F_{\beta_{u_y}}(z_p)u_{y\beta_{u_y}}^{p,k}(x,y,t) & \beta_{u_y} = 0,1,\dots,N_{u_y}^k \\ u_z^{p,k}(x,y,z_p,t) = F_{\beta_{u_z}}(z_p)u_{z\beta_{u_z}}^{p,k}(x,y,t) & \beta_{u_z} = 0,1,\dots,N_{u_z}^k \end{cases} \tag{24}$$

where summation is implied over the repeated indexes β_{u_s}. The term $F_{\beta_{u_s}}$ defines the set of thickness functions in terms of the ply coordinate z_p, $u_{r\beta_{u_s}}^{p,k}$ are the kinematic variables of the 2-D approximation of the p-th ply of the k-th sublaminate, and $N_{u_s}^k$ are the orders of expansion of the displacement components. The thickness functions are constructed as linear combinations of Legendre polynomials, as outlined in [38], so that all the functions but one vanish at the upper and lower interfaces:

$$\text{at } \zeta_p = 1 \quad \begin{cases} F_0 = 1 \\ F_{\beta_{u_s}} = 0 \qquad \beta_{u_s} = 1,\dots,N_{u_s}^k \end{cases} \tag{25}$$

and:

$$\text{at } \zeta_p = -1 \quad \begin{cases} F_1 = 1 \\ F_{\beta_{u_s}} = 0 \qquad \beta_{u_s} = 0,2,\dots,N_{u_s}^k \end{cases} \tag{26}$$

From Eqs. (25) and (26), it follows that the kinematic variables associated with the non-vanishing trial functions are the displacements at the top and bottom interfaces. In particular:

$$\begin{aligned} u_s^{p,k}(\zeta_p = +1) &= u_s^{p,k-\text{top}} = u_{s0}^{p,k} \\ u_s^{p,k}(\zeta_p = -1) &= u_s^{p,k-\text{bot}} = u_{s1}^{p,k} \end{aligned} \tag{27}$$

The assembly procedure between sublaminates is thus straightforward and, specifically, can be conducted in a layer-wise manner.

A compact notation is introduced, where $\text{ED}_{N_{u_x},N_{u_y},N_{u_z}}$ defines an ESL theory and $\text{LD}_{N_{u_x},N_{u_y},N_{u_z}}$ a LW theory of orders N_{u_x}, N_{u_y}, N_{u_z}. Whenever the same expansion of order N is adopted for the three displacement components, the acronym is shortened to ED_N or LD_N.

The PVD is expressed as function of the kinematic variables $u^{p,k}_{s\beta_{u_s}}$ by substituting the expansion of Eq. (24) into Eqs. (19)-(23).

The resulting expression, not repeated here for the sake of brevity, provides the displacement-based variational statement embedding the kinematic S-GUF description. An approximate solution is sought by referring to the Ritz method, as discussed in the following section.

It is worth clarifying the concept of theory-related DOFs, which is used hereinafter as a metric for assessing the cost associated with the kinematic models. Specifically, they reflect the number of generalized displacement components approximating the displacement field, and are evaluated by: (i) counting the number of layers where a different kinematic theory is used; this number is obtained as the sum of the sublaminates described in an ESL manner plus the number of plies modeled with a LW approach; (ii) counting the number of kinematic variables, that is $3 + N_{u_x} + N_{u_y} + N_{u_z}$, for each of those layers; (iii) subtracting the number of continuity conditions, equals 3 times the number of layer interfaces. Based on these considerations, the expression is obtained as:

$$\text{DOFs} = 3 + \sum_{k:ESL} N^k_{u_r} + \sum_{k:LW} N_k N^k_{u_r} \tag{28}$$

2.3 The in-plane approximation

The Ritz approximation consists in expressing each kinematic variable as a linear combination of appropriate spatial functions, namely:

$$\begin{cases} u^{p,k}_{x\beta_{u_x}}(x,y,t) = N_{u_x j}(x,y)\,u^{p,k}_{x\beta_{u_x} j}(t) \\ u^{p,k}_{y\beta_{u_y}}(x,y,t) = N_{u_y j}(x,y)\,u^{p,k}_{y\beta_{u_y} j}(t) \\ u^{p,k}_{z\beta_{u_z}}(x,y,t) = N_{u_z j}(x,y)\,u^{p,k}_{z\beta_{u_z} j}(t) \end{cases} \qquad j = 1, 2, \ldots, M \tag{29}$$

where $N_{u_s 1}, N_{u_s 2}, \ldots, N_{u_s M}$ is a complete set of global, admissible and linearly independent trial functions. For simplicity, the same number M of Ritz functions is adopted for all the displacement components. It is remarked that the trial functions have no ply or sublaminate dependence.

The trial set is taken as the product between boundary functions, introduced to fulfill the essential boundary conditions, and a combination of orthogonal polynomials. Specifically, Legendre polynomials are considered due to their excellent convergence and stability properties. Furthermore, they guarantee the highest sparsity of the resulting matrices [43] which is beneficial in terms of cost of the solution process.

The virtual variations of the displacement components are also approximated in a similar fashion, according to Eqs. (24) and (29).

2.4 The thickness and Ritz integrals

After inserting the Ritz approximation into the variational statement, the through-the-thickness and in-plane integrals can be computed independently from each other. A compact notation is introduced for the z- and Ω-integrals, which are written as:

$$Z^{p\alpha_{u_r}\beta_{u_s}}_{(\partial)u_r(\partial)u_s dn} = \int_{z_p^{\mathrm{bot}}}^{z_p^{\mathrm{top}}} \frac{R^n}{(R+z)^d} F_{\alpha_{u_r}(,z)} F_{\beta_{u_s}(,z)} \left(1+\frac{z_p}{R}\right) \mathrm{d}z_p \qquad (d,n=0,1,2) \tag{30}$$

and:

$$\mathcal{I}^{defg}_{u_r u_s ij} = \int_\Omega \frac{\partial^{d+e} N_{u_r i}}{\partial x^d \partial y^e} \frac{\partial^{f+g} N_{u_s j}}{\partial x^f \partial y^g} \mathrm{d}\Omega \qquad (d,e,f,g=0,1) \tag{31}$$

The expressions of Eqs. (30) and (31) are of general validity and represent any possible combination of thickness and Ritz functions, making it possible to express the PVD compactly as:

$$\begin{aligned} &\sum_{k=1}^{N_k} \sum_{p=1}^{N_p^k} \delta u^{p,k}_{r\alpha_{u_r}i} \tilde{C}^{p,k}_{RS} Z^{p\alpha_{u_r}\beta_{u_s}}_{(\partial)u_r(\partial)u_s dn} \mathcal{I}^{defg}_{u_r u_s ij} u^{p,k}_{s\beta_{u_s}j} + \\ &+ \sum_{k=1}^{N_k} \sum_{p=1}^{N_p^k} \delta u^{p,k}_{r\alpha_{u_r}i} \rho^{p,k} Z^{p\alpha_{u_r}\beta_{u_r}}_{u_r u_r} \mathcal{I}^{0000}_{u_r u_r ij} \ddot{u}^{p,k}_{r\beta_{u_r}j} = \\ &= \delta u^{N_p^k,N_k}_{z0i} \mathcal{I}^{\mathrm{top}}_{u_z f_z i} f_0^{\mathrm{top}} + \delta u^{1,1}_{z1i} \mathcal{I}^{\mathrm{bot}}_{u_z f_z i} f_0^{\mathrm{bot}} \end{aligned} \tag{32}$$

where:

$$\mathcal{I}^{\mathrm{top}}_{u_z f_z i} = \int_\Omega N_{u_z i} f^*_{\mathrm{top}} \left(1+\frac{h}{2R}\right) \mathrm{d}\Omega \qquad \mathcal{I}^{\mathrm{bot}}_{u_z f_z i} = \int_\Omega N_{u_z i} f^*_{\mathrm{bot}} \left(1-\frac{h}{2R}\right) \mathrm{d}\Omega \tag{33}$$

and:

$$f_z^{\mathrm{top}}(x,y,t) = f^*_{\mathrm{top}}(x,y) \cdot f_0^{\mathrm{top}}(t) \qquad f_z^{\mathrm{bot}}(x,y,t) = f^*_{\mathrm{bot}}(x,y) \cdot f_0^{\mathrm{bot}}(t) \tag{34}$$

The full expression of the discretized PVD is provided in the Appendix.

2.5 Expansion and assembly

The indicial form of the discretized PVD of Eq. (32) is expanded over the theory-related indexes in order to assemble the contributions at ply-sublaminate levels. By exploiting the properties of the thickness functions – see Eqs. (25) and (26) –, the compatibility between adjacent sublaminates can be enforced in a strong form manner. The assembly process can be graphically illustrated by organizing the thickness functions in two-dimensional arrays, as illustrated in Figure 2, where, for clarity, an example is presented regarding a three-sublaminate model based on theory LD$_3$/ ED$_3$/ ED$_1$. As seen form the figure, the contributions of the three sublaminates are characterized by arrays with different dimensions, consistently with the corresponding kinematic theories. The compatibility requirements involve just the kinematic variables at the top and the bottom of each sublaminate. Therefore, they are easily enforced by assembling the contributions, as sketched in Figure 2. Note, the procedure is independent on the kind of theories employed, and the assembly is conducted in the very same way for ED/ED, LD/LD and ED/LD interfaces. Further details of the procedure can be found in [38], where the S-GUF-Ritz method was developed for flat plates. Following similar steps, the PVD takes the form:

$$\delta \mathbf{u}^{\mathrm{T}} \mathbf{M} \ddot{\mathbf{u}} + \delta \mathbf{u}^{\mathrm{T}} \mathbf{K} \mathbf{u} = \delta \mathbf{u}^{\mathrm{T}} \mathbf{L} \qquad \forall\, \delta \mathbf{u} \tag{35}$$

where $\mathbf{u}$ collects the unknown amplitudes of the kinematic variables, $\mathbf{K}$ is the stiffness matrix, $\mathbf{M}$ is the mass matrix and $\mathbf{L}$ is the load vector.

Free vibration and bending equations are obtained exploiting the arbitrariness of the virtual displacements $\delta\mathbf{u}$ and either setting the external loads to zero or removing the time-dependence, respectively. The algebraic solution of such problems provides the amplitudes of the kinematic variables that are post-processed to recover the physical quantities of interest such as displacements, stresses and strains.

2.6 Stress recovery

The accurate evaluation of the internal stresses is a crucial aspect during the analysis process. In particular, in-plane components are relevant for checking intra-laminar fibre and matrix failures, whilst transverse components are of paramount importance for predicting inter-laminar failure mechanisms such as delamination. In the framework of a classical displacement-based approach, the stresses are available by application of the Hooke's law which, in turn, makes use of the strains available by differentiation of the displacement components. In the present implementation distinction is made between in-plane and transverse stress components. The former are obtained referring to the Hooke's law, the latter by integration of the equilibrium equations. As a matter of fact, the process of integrating the equilibrium equations allows to recover accurate information regarding the transverse shear stresses, even in the presence of kinematic theories of relatively low order along z.

The process of integration of the equilibrium equations is carried out by referring to the elementary volume in cylindrical coordinates depicted in Figure 3. The coordinate system to describe the element is the axial-tangential-radial (x, ϕ, ρ). In this reference system, the equilibrium equations read:

$$\begin{cases} \dfrac{\partial \sigma_x}{\partial x} + \dfrac{1}{\rho}\dfrac{\partial \tau_{x\phi}}{\partial \phi} + \dfrac{\partial \tau_{x\rho}}{\partial \rho} + \dfrac{\tau_{x\rho}}{\rho} = 0 \\ \dfrac{\partial \tau_{\phi x}}{\partial x} + \dfrac{1}{\rho}\dfrac{\partial \sigma_{\phi}}{\partial \phi} + \dfrac{\partial \tau_{\phi\rho}}{\partial \rho} + 2\dfrac{\tau_{\phi\rho}}{\rho} = 0 \\ \dfrac{\partial \tau_{\rho x}}{\partial x} + \dfrac{1}{\rho}\dfrac{\partial \tau_{\rho\phi}}{\partial \phi} + \dfrac{\partial \sigma_{\rho}}{\partial \rho} + \dfrac{\sigma_{\rho}}{\rho} - \dfrac{\sigma_{\phi}}{\rho} = 0 \end{cases} \tag{36}$$

The previous equation is reduced to an easier-to-integrate version by observing that:

$$\frac{\partial f(\rho)}{\partial \rho} + n\frac{f(\rho)}{\rho} = \frac{1}{\rho^n}\frac{\partial}{\partial \rho}\left(\rho^n f(\rho)\right) \tag{37}$$

In addition, the following change of variables is performed:

$$\begin{aligned} \rho &= z + R && \Rightarrow && \mathrm{d}\rho = \mathrm{d}z \\ \phi &= \frac{y}{R} && \Rightarrow && \mathrm{d}\phi = \frac{1}{R}\mathrm{d}y \end{aligned} \tag{38}$$

Using Eq. (37) and (38), it is possible to rewrite Eq. (36) as:

$$\begin{cases} \left(1+\dfrac{z}{R}\right)\dfrac{\partial \sigma_x}{\partial x} + \dfrac{\partial \tau_{xy}}{\partial y} + \dfrac{\partial}{\partial z}\left[\left(1+\dfrac{z}{R}\right)\tau_{xz}\right] = 0 \\ \left(1+\dfrac{z}{R}\right)^2 \dfrac{\partial \tau_{xy}}{\partial x} + \left(1+\dfrac{z}{R}\right)\dfrac{\partial \sigma_y}{\partial y} + \dfrac{\partial}{\partial z}\left[\left(1+\dfrac{z}{R}\right)^2 \tau_{yz}\right] = 0 \\ \left(1+\dfrac{z}{R}\right)\dfrac{\partial \tau_{xz}}{\partial x} + \dfrac{\partial \tau_{yz}}{\partial y} + \dfrac{\partial}{\partial z}\left[\left(1+\dfrac{z}{R}\right)\sigma_z\right] - \dfrac{\sigma_y}{R} = 0 \end{cases} \tag{39}$$

The equilibrium conditions given by Eq. (39) are integrated along-the-thickness starting from the inner side, where the internal stresses are set equals to the applied load, namely:

$$\begin{aligned} \left(1+\frac{z}{R}\right)\tau_{xz}(z) &= -\int_{-h/2}^{z}\left[\left(1+\frac{s}{R}\right)\frac{\partial \sigma_x(s)}{\partial x} + \frac{\partial \tau_{xy}(s)}{\partial y}\right]\mathrm{d}s \\ \left(1+\frac{z}{R}\right)^2\tau_{yz}(z) &= -\int_{-h/2}^{z}\left[\left(1+\frac{s}{R}\right)^2\frac{\partial \tau_{xy}(s)}{\partial x} + \left(1+\frac{s}{R}\right)\frac{\partial \sigma_y(s)}{\partial y}\right]\mathrm{d}s \\ \left(1+\frac{z}{R}\right)\sigma_z(z) &= f_z^{\mathrm{bot}} - \int_{-h/2}^{z}\left[\left(1+\frac{s}{R}\right)\frac{\partial \tau_{xz}(s)}{\partial x} + \frac{\partial \tau_{yz}(s)}{\partial y} - \frac{\sigma_y(s)}{R}\right]\mathrm{d}s \end{aligned} \tag{40}$$

where s is a dummy integration variable. Note that, according to the sublaminate description of the shell, the integrals in Eq. (40) are performed ply-by-ply. For instance, the evaluation of the stress components within the P-th ply of the K-th sublaminate involves the computation of integrals in the form of:

$$\int_{-h/2}^{z} f(s)\mathrm{d}s = \sum_{k=1}^{K-1}\sum_{p=1}^{N_p^k}\int_{z_p^{\mathrm{bot}}}^{z_p^{\mathrm{top}}} f^{p,k}(z_p)\mathrm{d}z_p + \sum_{p=1}^{P-1}\int_{z_p^{\mathrm{bot}}}^{z_p^{\mathrm{top}}} f^{p,K}(z_p)\mathrm{d}z_p + \int_{z_P^{\mathrm{bot}}}^{z_P} f^{P,K}(z'_P)\mathrm{d}z'_P \tag{41}$$

Note that the evaluation of σ_z (see the last of Eq. (40)) requires the computation of the first derivatives of τ_{xz} and τ_{xy} with respect to the x and y coordinates, respectively, which are obtained as:

$$\begin{aligned} \left(1+\frac{z}{R}\right)\frac{\partial \tau_{xz}(z)}{\partial x} &= -\int_{-h/2}^{z}\left[\left(1+\frac{s}{R}\right)\frac{\partial^2 \sigma_x(s)}{\partial x^2} + \frac{\partial^2 \tau_{xy}(s)}{\partial x \partial y}\right]\mathrm{d}s \\ \left(1+\frac{z}{R}\right)^2\frac{\partial \tau_{yz}(z)}{\partial y} &= -\int_{-h/2}^{z}\left[\left(1+\frac{s}{R}\right)^2\frac{\partial^2 \tau_{xy}(s)}{\partial x \partial y} + \left(1+\frac{s}{R}\right)\frac{\partial^2 \sigma_y(s)}{\partial y^2}\right]\mathrm{d}s \end{aligned} \tag{42}$$

The integrals of Eqs. (40) and (42) are computed numerically with a 4^{th} order Newton-Cotes rule, which provides a good trade-off between computational cost and accuracy.

3 Results

In this section, the results obtained using the S-GUF-Ritz approach are presented. Specifically, the section is organized in two parts. In the first part, two test cases from the literature, i.e. a conventional sandwich panel with laminate skins and a double-core sandwich panel, are analyzed for validation purposes. The second example, due to its unconventional configuration, is believed of particular interest to highlight the flexibility of employ of the present formulation, which is not restricted to classical skin/core/skin architectures. In the second part of the section, novel results are provided for innovative helicopter trim panels investigated by the authors within the *Helicopter Garteur Action Group AG-20* [7]. The three-core configuration of these panels provides an interesting, real-life example, where classical sandwich theories may fail at capturing the complex mechanical response of the structure. In this sense, the corresponding results can be taken as a useful benchmark for future investigations in the field of sandwich panels.

3.1 Comparison with reference results

Example 1: Free-vibrations of single-core sandwich shell

The first test-case deals with the free vibration response of a sandwich shell composed by two skins and one core. The configuration is taken from Ref. [44], where exact 3D elasticity solutions are derived and considered here for comparison purposes.

The geometry of the shell is characterized by $R = 10\ m$, and $a = 20\ m$, and $b/R = \pi/3$. According to this latter parameter, the shell can be classified as deep. The radius-to-thickness ratio R/h is varied to consider both thin and thick configurations. In particular, it can take the values 5, 10, 100 and 1000, while the non-dimensional thickness of the core h_c/h is equal to 0.7. The composite skins are layered with the cross-ply stacking sequence [90/0], where the outer plies are those oriented at 90 degrees. They are made of graphite/epoxy material, while the core is a soft PVC foam. The mechanical properties of the two materials are reported in Table 1, and are denoted as Skin-1 and Core-1. Simply-supported boundary conditions are considered at the four edges.

The analyses are conducted by dividing the stack into three sublaminates, as suggested by the skin/core/skin configuration of the panel. With this regard, this sublaminate model follows the classical strategy employed by sandwich theories available in the literature, such as high-order sandwich panel theory (HSAPT) [36] or extended sandwich plate theory (EHSAPT) [45], which make use of a combination of kinematic theories for modeling the two faces and the core. However, the present formulation is not restricted to a specific set of pre-defined kinematic models, as they can be defined arbitrarily, depending on the problem at hand. In this case, a model ED_2/ ED_4/ ED_2 was found as adequate for providing accurate predictions and properly capturing the relatively complex through-the-thickness behaviour. The total number of theory-related degrees of freedom is equal to 27. A number of 25×25 trial functions is taken for approximating the in-plane behaviour.

The results are summarized Table 2, where the non-dimensional circular frequencies $\hat{\omega}_{m,n}$ are presented for different radius-to-thickness ratios. The subscript letters m and n denote the number of half-waves along the axial and tangential directions, respectively. The roman numerals (I to III) are introduced in the table to distinguish between eigenmodes sharing equal planar shape, but different thickness-wise behaviour.

The comparison reveals close agreement between 3D and S-GUF predictions, with percent differences below 0.1% for all the cases reported. It is interesting to observe that the quality of results is insensitive to the radius-to-thickness ratio, and high accuracy is demonstrated even in the case of thick shells with $R/h = 5$. It can be noted that modes with equal planar shapes are much more separated in the case of thin shells, i.e. $R/h = 1000$, while they tend to get closer when the shell thickness is increased. For instance, modes II and III are, approximately, 26 and 14 times higher than mode I for the combination of half-waves (1,1) and R/h equal to 1000. On the contrary, they are only 6 and 8 times higher when the ratio R/h is reduced to 5. This result further highlights the importance of adopting sufficiently rich kinematic models for thick shells, even when the frequency range of interest is not necessarily extended to high frequencies.

In addition, one can note the influence of the radius-to-thickness ratio on the relative order of the modes I, II and III. For instance, mode (1,2)-I is observed at a higher frequency than modes (1,1)-I and (2,1)-I for $R/h = 5$. The opposite trend is seen for $R/h = 1000$. Similar conclusions, although characterized by a different relative pattern, can be drawn for modes II and III.

Interestingly, modes II are detected at about the same non-dimensional frequency $\hat{\omega} \simeq 18$ for the thick shell with $R/h = 5$, irrespective of the number of half-waves along each direction.

The through-the-thickness behaviour corresponding to the modes with (2,2) half-waves is illustrated in Figure 4 for a shell characterized by R/h equal to 10. The modes are scaled to maximum unitary displacement and the comparison is presented with the results derived by Brischetto [44]. The first of the three modes shows a displacement field characterized by piece-wise linear displacement components u_x and u_y, while u_z is constant. In this case a low order sublaminate theory, e.g $\text{ED}_{1,1,0}$/ $\text{ED}_{1,1,0}$/ $\text{ED}_{1,1,0}$, would suffice for grasping the kinematic field with a good degree of accuracy. On the contrary, the modes II and III exhibit more complex patterns, which force the adoption of more refined thickness-wise descriptions. For this reason, the availability of a model capable of combining any arbitrary kinematic theory can be advantageous: depending on the needs, the analyst can keep at minimum the number of theory-related degrees of freedom, enriching the kinematic description only when this is strictly needed.

Example 2: Bending of double-core sandwich shell

The second test-case deals with the bending analysis of a sandwich shell with two cores and three skins, for which exact 3D results are reported by Yasin and Kapuria [46]. This configuration is of particular interest due to its unconventional arrangement, which makes classical sandwich theories, specifically developed for the single core case, not adequate. On the contrary, the proposed S-GUF approach is versatile enough to allow the description of any arbitrary through-the-thickness configuration and, therefore, can be successfully applied.

Specifically, the shell is shallow and characterized by a width-to-radius ratio b/R equal to 0.5. Thick and moderately thick configurations are analyzed by considering thickness ratios b/h of 5 and 10, respectively, while the aspect ratio a/b is set equal to 1 and 2. Each core has a relative thickness h_c/h of 0.4325, while the three skins are characterized by equal thickness, corresponding to the non-dimensional value h_s/h of 0.045. Material properties of skins and cores are summarized in Table 1, and are indicated as Skin-2 and Core-2. The stacking sequence of the panel is (90/0/90/core/90/0/90/core/90/0/90). The shell is simply-supported at the four edges and is subjected to a bi-sinusoidally distributed pressure load of intensity f_0 acting at the outer surface.

The results are reported in Table 3 in terms of non-dimensional displacement and stress components, evaluated at different spots inside the structure. The caret is introduced to denote the non-dimensional parameters, which are defined as:

$$\hat{u}_r = 100\frac{E_2^{\mathrm{face}}}{h(b/h)^4 f_0}u_r \qquad \hat{\sigma}_r = \frac{1}{(b/h)^2 f_0}\sigma_r \qquad \hat{\tau}_{xy} = \frac{10}{(b/h)^2 f_0}\tau_{xy} \qquad (\hat{\tau}_{xz}, \hat{\tau}_{yz}) = \frac{1}{(b/h) f_0}(\tau_{xz}, \tau_{yz}) \tag{43}$$

The ease in realizing different kinematic models is exploited to highlight the effect of considering different theories along with their accuracy in comparison to the exact results. In particular, two layer-wise and one equivalent single layer descriptions are considered.

From Table 3 one can observe that the fourth-order layer-wise theory $\mathrm{LD}_{4,4,3}$ guarantees quasi-3D predictions, as agreement is observed with the exact solution, in all but one case, up to the first four digits, the highest error being equal to 0.4%. Clearly, the disadvantage of this approach relies in the large number of theory-related degrees of freedom, which is equal to 124. A reduction of the theory's order to $\mathrm{LD}_{1,1,0}$ – which is, as a matter of fact, a layer-wise FSDT description – leads to 25 theory-related degrees of freedom, but errors as high as 6.8%. Alternatively, the adoption of a high order equivalent single layer model $\mathrm{ED}_{7,7,6}$ provides further reduction to 23 degrees of freedom, but maximum errors close to 9%. In this case, the inaccuracy is exacerbated by the inability of the homogenized model to capture the slope discontinuities experienced by the displacement field at the core-face interfaces.

An excellent trade-off between accuracy and number of degrees of freedom can be achieved by taking advantage of the sublaminate capabilities of the S-GUF approach. The structure is divided into five sub-regions, as suggested by the sandwich configuration, where each core and skin correspond to one single sublaminate. Specifically, the model S-GUF of Table 3 considers the combination of kinematic theories $\mathrm{ED}_{2,2,1}$/ $\mathrm{ED}_{3,3,2}$/ $\mathrm{ED}_{2,2,1}$/ $\mathrm{ED}_{3,3,2}$/ $\mathrm{ED}_{2,2,1}$, where higher-order descriptions are introduced to capture the higher degree of non-linearity exhibited by the displacement field in correspondence of each weak core. It is worth noting that the sublaminate formulation allows for a piecewise polynomial description of the displacement field, therefore any zig-zag effect is inherently captured by the proposed description. The total number of degrees of freedom is equal to 34, approximately one third of those associated with the $\mathrm{LD}_{4,4,3}$ approach, but still guarantees a similar level of accuracy.

The quality of the S-GUF predictions can be further investigated by assessing the through-the-thickness behaviour of displacement and stress components at selected locations of the shell, as illustrated in Figures 5-7 for the thick shell with unitary aspect ratio. For clarity, gray regions are depicted in the plots in correspondence of the skin layers, and a red dot is reported in the panel's sketch to indicate the evaluation point. The results obtained with S-GUF models are checked against those computed with $\text{LD}_{4,4,3}$, this latter taken as a reference due to its quasi-3D capabilities. Furthermore, FSDT and $\text{ED}_{7,7,6}$ predictions are reported for providing additional comparison.

The advantages offered by the sublaminate formulation are clearly established by inspection of Figure 5, where the axial and circumferential displacements are reported. The almost identical description offered by the $\text{LD}_{4,4,3}$ and S-GUF approach can be observed. On the contrary, the discontinuities of the first derivative of the displacement are not captured by the high order theory $\text{ED}_{7,7,6}$, which is then responsible for large inaccuracies. Some meaningful stress components predictions are depicted in Figures 6 and 7. It is interesting to remark the differences in terms of transverse shear stress distributions, where the ESL theories FSDT and $\text{ED}_{7,7,6}$ are clearly deviated from the quasi-3D results of $\text{LD}_{4,4,3}$ despite the stress recovery process performed via integration of the equilibrium equations. On the contrary, the predictions available using the S-GUF model are almost indistinguishable from the layer-wise ones.

3.2 Analysis of triple-core helicopter trim panels

This section is devoted to the analysis of innovative sandwich configurations characterized by a non-conventional architecture with three cores. These panels were the subject of a research activity carried out as part of the *Helicopter Garteur Action Group AG-20*, aimed at improving the acoustic comfort inside helicopter cabins [7]. The motivations for presenting these results are twofold: firstly, illustrating real-life applications that could benefit from the availability of an analysis tool capable of handling any kind of skin/core lay-out, providing complete freedom in defining the structural model in terms of sublaminate description as well as order of the kinematic theories; secondly, providing results for benchmarking purposes, given the inherent complexity of the triple-core configuration.

A sketch of the panel is reported in Figure 8, where the arrangement of the stack is shown. The configuration is symmetric, and is characterized by the presence of a central foam core bonded to two outer Nomex cores and two external skins made of a four-ply glass fabric laminate. The mechanical properties are available in Table 4 along with the thicknesses of the 13 layers composing the stack.

The panel is square with planar dimensions of 840 mm and total thickness equal to 21.68 mm, corresponding to a non-dimensional ratio b/h of approximately 39. Therefore, the panel is just moderately thick, but the drastic through-the-thickness heterogeneity renders the analysis particularly challenging. The boundary conditions are approximated as fully clamped to simulate the experimental fixture.

Firstly, the results are presented by considering the typical flat geometry of helicopter trim panels, as the ones analyzed and tested within the *Garteur* project. Then, the analysis is extended to the case of cylindrically curved panels, which can be representative of those employed in the context of aircraft fuselage structures.

Flat configuration

The natural dimensional frequencies are plotted versus the mode number in Figure 9, where the comparison is illustrated between S-GUF predictions and results of modal tests conducted at ONERA. A detailed description of the experimental activity can be found in Ref. [41, 47].

The numerical models are based on the sublaminate scheme $\mathrm{ED}_{1,1,0}$/ $\mathrm{LD}_{1,1,0}$/ $\mathrm{ED}_{3,3,2}$/ $\mathrm{LD}_{1,1,0}$/ $\mathrm{ED}_{1,1,0}$ theory. It is worth noting that this choice is not unique and does not necessarily represent the most effective one in terms of accuracy-to-degrees of freedom ratio. However, it is a satisfactory combination that guarantees accurate results, as revealed by preliminary studies, with a relatively low computational effort.

The definition of the model is lead by engineering considerations, illustrated here below to provide further insight into the handling of the modeling flexibility offered by the S-GUF approach. Specifically:

- the outer glass fiber layers are thin and stiff, therefore the first-order kinematic model $\mathrm{ED}_{1,1,0}$, i.e. FSDT, is a natural choice to guarantee an adequate description;
- the Nomex core and the glue layer are merged into one single sublaminate, where $\mathrm{LD}_{1,1,0}$ is employed. In this case, a layer-wise approach is preferred due to noticeable differences between the mechanical properties of the two materials. Note that inextensibility is assumed along the thickness direction as this effect is not particularly relevant for both layers. Indeed, the glue layer is very thin, while the Nomex is characterized by relatively high stiffness in the thickness direction;
- the foam core is soft and demands for a high-order description. A third-order theory $\mathrm{ED}_{3,3,2}$ is thus a natural choice. Note that the second-order description along the thickness direction offers the chance to grasp thickness-wise extension/contraction effects, which can be relevant due to the weak core properties.

Experimental values were determined up to 300 Hz, while numerical analyses are run to assess the panel response up to 1 kHz. The zoom in Figure 9 highlights the comparison between experimental and numerical values. A good agreement is observed. Some deviations can be noticed as the frequency increases due to several sources of uncertainty, including non-ideal boundary conditions of the experimental set-up, as well as unavoidable deviations between nominal and actual elastic properties of the material.

The numerical curves are reported for different number of trial functions, from 18 to 26 along the directions x and y. It can be seen that the results are almost superposed in the low frequency range, while they tend to diverge for relatively high frequency values, due to the increasingly shorter size of the half-waves. However, the formulation is so efficient that a large number of trial functions, if needed, can be handled with relative ease.

An abrupt change of slope is observed in the curve at approximately 620 Hz, which is associated with the presence of thickness modes. To clarify this aspect, a zoom of the modes 70 to 130 – those in the neighborhood of the discontinuity – is reported in Figure 10. Before the change of slope, i.e. on the left of the vertical line, the modal patterns do not exhibit any stretching/contraction along the thickness direction, and the length of the half-waves becomes increasingly shorter. Some representative cases are reported in the top of the figure, beyond the predicted frequency values. After crossing the vertical line, the modal density is higher due to the onset of eigenmodes characterized by thickness-wise stretching/contraction and in-plane response with long half-waves, examples of which are presented at the bottom of the figure. In this case, the planar shape resembles that of the first eigenmodes. However, the thickness behaviour is drastically different, as shown in Figure 11, where the comparison is presented between modes 1 and 2, and modes 93 and 94.

Cylindrically curved configuration

It is interesting to extend the analysis to the case of cylindrically curved shells, while retaining the same configuration in terms of stacking sequence and materials. In particular, the effect of curvature is assessed by varying the side-to-radius ratio b/R, ranging from the limiting case of flat panel ($b/R = 0$) to that of a very deep shell ($b/R = 2$). In addition, different values for the panel width-to-thickness ratio b/h are considered in the range between 5 and 100, i.e. from very thick to thin configurations.

By analogy with the flat plate case, the same S-GUF model is considered, which is $\mathrm{ED}_{1,1,0}$/ $\mathrm{LD}_{1,1,0}$/ $\mathrm{ED}_{3,3,2}$/ $\mathrm{LD}_{1,1,0}$/ $\mathrm{ED}_{1,1,0}$. The total number of theory-related DOFs is 23, while a 128-DOF layer-wise $\mathrm{LD}_{4,4,3}$ model is employed for comparison purposes due to its quasi-3D capabilities. FSDT theory is used to model the thin glue layer.

The natural frequencies are summarized in Table 5 for several combinations of geometrical parameters, including the ratio $b/h = 38.75$ corresponding to the original panel.

Close agreement is observed between the two models with percent differences ranging from 1% for the very thick panels with $b/h = 5$, to 0.01% for the thin panel with $b/h = 100$, irrespective of the b/R ratio. The small differences between the two models provide further evidence of the excellent accuracy-to-DOF ratio offered by the S-GUF approach. The full layer-wise model $\mathrm{LD}_{4,4,3}$ is associated with five times the number of DOFs, with no appreciable advantages in terms of quality of the predictions.

The effect of changing the curvature radius is further assessed in Figure 12, where the fundamental frequency is plotted against the width-to-radius ratio for in-plane dimensions equal to 840 mm. The curve reports also the strain energy ratio $U_\Omega/U_{\mathrm{tot}}$, where U_{tot} is the total strain energy, while U_Ω is the in-plane contribution, calculated as:

$$U_\Omega = \int_\Omega \int_{-h/2}^{h/2} \boldsymbol{\varepsilon}_\Omega^{\mathrm{T}} \boldsymbol{\sigma}_\Omega \mathrm{d}z\, \mathrm{d}\Omega \tag{44}$$

Clearly, the amount of strain energy due to transverse shear and normal deformation is readily available as $U_{\mathrm{n}} = 1 - U_{\Omega}$.

As seen from the plot, the dimensional frequency increases as the shell becomes deeper, a behaviour which is accompanied by an increasing amount of the membrane energy contribution. In other words, the effect of curving the panel is that of promoting its membrane energy response in spite of the transverse shear one. As a matter of fact, the amount of membrane strain energy is 45% and 93% when the shell is shallow, ($b/R = 0.01$) and very deep ($b/R = 5$), respectively. A set of discontinuity points can be observed with respect to the slope of the frequency curve, which correspond to the presence of two coincident eigenvalues. Across these points, a modal transition is experienced by the shell. As revealed by the shapes in the figure, the eigenmode undergoes a change of pattern by progressively increasing the number of circumferential half-waves as the shell becomes deeper. It is worth mentioning that the modal transitions are associated with a sudden drop of the membrane energy, which is converted into transverse shear and normal one.

Trim panels are primarily designed under acoustic requirements, and they are generally not subjected to noticeable static loads. However, given the complexity and heterogeneity of their composition, it is interesting to illustrate their bending response, which can be taken as a challenging benchmark for future comparisons. The loading condition considered here is a uniformly distributed pressure of magnitude $f_0 = 10$ kPa acting at the outer surface. The in-plane dimensions are 840 mm, while the ratio b/R ranges from 0 to 2; fully clamped and simply-supported boundary conditions are assumed. A number of relevant results is collected in Table 6, including the normal microstrains $\mu\varepsilon_z$, the in-plane stresses $\hat{\sigma}_x$ and $\hat{\sigma}_y$, and the transverse shear one $\hat{\tau}_{xz}$. The caret is introduced to denote non-dimensional values, obtained as $\hat{\sigma}_i = \sigma_i/f_0$ and $\hat{\tau_{ik}} = \tau_{ik}/f_0$. Note, the accurate evaluation of the transverse shear stress components at the clamped edges requires a relatively large number of functions due to noticeable spatial gradients of the displacement field close to the boundaries. A preliminary convergence analysis, not reported here for the sake of conciseness, proved 50×50 functions as adequate for providing accurate results. From Table 6, it is noted that stress and strain magnitudes decrease with the side-to-radius ratio, due to the stabilizing effect provided by the bending/membrane coupling, consistently with the behaviour experienced in the free vibration case. A slight increment of traction stresses in the upper face is nonetheless detected for shallow shells, accompanied by steep decrements of compression stresses in the lower face. It is also observed that, for deep enough shells, traction stresses are present both in the inner and outer faces.

Displacement and stress components are also shown for the fully clamped deep shell with $b/R = 1$ in Figures 13-15. The panel is depicted along with the loading condition and a red dot shows the evaluation points.

The results predicted using S-GUF models are presented in comparison with those obtained using FSDT, $\mathrm{ED}_{7,7,6}$ and $\mathrm{LD}_{4,4,3}$. As revealed by the results, first-order and high-order ESL theories are unable to properly capture the mechanical response of the panels, mainly due to the high compliance of the thick central core and the corresponding mismatch of mechanical properties among the layers. It is interesting to note that, even though a sixth-order polynomial is used for the z-component in $\mathrm{ED}_{7,7,6}$, the radial displacement is predicted as almost constant through-the thickness.

The results obtained via S-GUF are almost indistinguishable from the ones of $\mathrm{LD}_{4,4,3}$, with a significant reduction of the theory-related DOFs, from 128 to 23. These results remark the capability of S-GUF to guarantee accurate results along with reduced computational cost, provided an adequate choice of the DOFs is performed.

4 Conclusions

The paper discussed the extension of the S-GUF Ritz formulation to the linear analysis of cylindrically curved shells. Due to the primary role played by cylindrical structures in many mechanical and aerospace applications, the extension represents an important step toward the development of a numerical tool for analyzing more realistic panel configurations.

The approach is developed in the framework of the S-GUF formulation, and approximate solutions are retrieved by referring to the method of Ritz. Main advantage of the proposed strategy relies in the possibility of modeling any configuration with the desired level of detail by properly combining the definition of the sublaminates along with the corresponding kinematic theories. The approach furnishes an easy and straightforward strategy even for analyzing non-conventional configurations with multiple cores, such as those employed in some modern aerospace applications, which could be hardly studied referring to classical sandwich theories.

The quality of the predictions is demonstrated by comparison with reference 3D solutions for single and double-core sandwich shells, demonstrating that quasi-3D accuracy can be guaranteed with a relatively small number of degrees of freedom, much less with respect to those required by a purely layer-wise approach.

The features offered by the S-GUF Ritz formulation are particularly useful during the design phase of complex sandwich shells, such as the triple-core panels discussed in the paper. Indeed, insight can be gathered into their mechanical behaviour with no need to realize complex and costly three dimensional models. Any geometric parameter and configuration arrangement can be investigated and modified on the fly. Bending and free-vibration results are presented, although the approach can be easily extended to any other mechanical and thermo-elastic solution procedure.

References

[1] J.R. Vinson. Sandwich structures: past, present and future. In O. Thomsen, E. Bozhevolnaya, and A. Lyckegaard, editors, *Sandwich structures 7: advancing with sandwich structures and materials*, pages 1–12. Springer, Dordecht, 2005.

[2] A.S. Herrmann, P.C Zahlen, and I. Zuardy. Sandwich structures technology in commercial aviation. In O. Thomsen, E. Bozhevolnaya, and A. Lyckegaard, editors, *Sandwich structures 7: advancing with sandwich structures and materials*, pages 13–26. Springer, Dordecht, 2005.

[3] H.F. Seibert. Applications for PMI foams in aerospace sandwich structures. *Reinforced Plastics*, 50(1):44–48, 2006.

[4] D.H. Hodges. Review of composite rotor blade modeling. *AIAA Journal*, 28(3):561–565, 1990.

[5] S. Kodiyalam, A. Nagendra, and J. De Stefano. Composite sandwich structure optimization with application to satellite components. *AIAA Journal*, 34(3):614–621, 1996.

[6] J.A. Moore and R.H. Lyon. Sound transmission loss characteristics of sandwich panel constructions. *The Journal of the Acoustical Society of America*, 89:777–791, 1991.

[7] F. Simon, T. Haase, O. Unruh, G.L. Ghiringhelli, A. Parrinello, and R. Vescovini. Benchmark for modelization of acoustic transmission loss applied to helicopter trim panels. In *42^{nd} European Rotorcraft Forum (ERF 2016)*, Lille, France, 5–8 September, 2016.

[8] R.K. Kapania. A review on the analysis of laminated shells. *Journal of Pressure Vessel Technology*, 11(2):88–96, 1989.

[9] A. Noor and W.S. Burton. Assessment of computational models for multilayered composite shells. *Applied Mechanics Reviews*, 43(4):67–97, 1990.

[10] M.S. Qatu, R.W. Sullivan, and W. Wang. Recent research advances on the dynamic analysis of composite shells: 2000–2009. *Composite Structures*, 93(1):14–31, 2010.

[11] M.F. Caliri, A.J.M. Ferreira, and V. Tita. A review on plate and shell theories for laminated and sandwich structures highlighting the Finite Element Method. *Composite Structures*, 2016(63–77), 156.

[12] H. Kraus. *Thin elastic shells: An Introduction to the Theoretical Foundations and the Analysis of Their Static and Dynamic Behavior.* John Wiley & Sons, 1967.

[13] J.N. Reddy. *Mechanics of Laminated Composite Plates and Shells: Theory and Analysis.* Boca Raton, Florida, US: CRC Press, 2^{nd} edition, 2004.

[14] J.N. Reddy and C.F. Liu. A higher-order shear deformation theory of laminated elastic shells. *International Journal of Engineering Science*, 23(3):319–330, 1985.

[15] S. Dennis and A.N. Palazotto. Transverse shear deformation in orthotropic cylindrical pressure vessels using a higher-order shear theory. *AIAA Journal*, 27(10):1441–1447, 1989.

[16] R.K. Khare, V. Rode, A.K. Garg, and S.P. John. Higher-order closed-form solutions for thick laminated sandwich shells. *Journal of Sandwich Structures & Materials*, 7(4):335–358, 2005.

[17] E. Carrera. Multilayered shell theories accounting for layerwise mixed description, part 1: Governing equations. *AIAA Journal*, 37(9):1107–1116, 1999.

[18] E. Carrera. Multilayered shell theories accounting for layerwise mixed description, part 2: Numerical evaluations. *AIAA Journal*, 37(9):1117–1124, 1999.

[19] Y. Başar and M.H. Omurtag. Free-vibration analysis of thin/thick laminated structures by layer-wise shell models. *Computers & Structures*, 74(4):409–427, 2000.

[20] K.Y. Lam, T.Y. Ng, and W. Qian. Vibration analysis of thick laminated composite cylindrical shells. *AIAA Journal*, 38(6):1102–1107, 2000.

[21] A.M.B. Braga and C.E. Rivas. High-frequency response of isotropic-laminated cylindrical shells modeled by a layer-wise theory. *International Journal of Solids and Structures*, 42(14):4278–4294, 2005.

[22] I. Sheinman and G.J. Simitses. Buckling analysis of geometrically imperfect stiffened cylinders under axial compression. *AIAA Journal*, 15(3):374–382, 1977.

[23] I. Sheinman, Y. Frostig, and A. Segal. PBCOMP program for buckling and postbuckling of stiffened laminated curved panels. *Computers & Structures*, 42(1):87–95, 1992.

[24] Y. Zhang and F.L. Matthews. Initial buckling of curved panels of generally layered composite materials. *Composite Structures*, 1(1):3–30, 1983.

[25] R. Vescovini and C. Bisagni. Buckling analysis and optimization of stiffened composite flat and curved panels. *AIAA Journal*, 50(4):904–915, 2012.

[26] A.K. Noor, W.S. Burton, and J.M. Peters. Assessment of computational models for multilayered composite cylinders. *International Journal of Solids and Structures*, 27(10):1269–1286, 1991.

[27] E. Carrera. A class of two-dimensional theories for anisotropic multilayered plates analysis. *Atti Accademia delle Scienze di Torino. Memorie Scienze Fisiche*, 19:1–39, 1995.

[28] E. Carrera. Theories and finite elements for multilayered plates and shells: a unified compact formulation with numerical assessment and benchmarking. *Archives of Computational Methods in Engineering*, 10(3):215–296, 2003.

[29] M. Cinefra and E. Carrera. Shell finite elements with different through-the-thickness kinematics for the linear analysis of cylindrical multilayered structures. *International Journal for Numerical Methods in Engineering*, 93(2):160–182, 2013.

[30] F. Tornabene, N. Fantuzzi, E. Viola, and E. Carrera. Static analysis of doubly-curved anisotropic shells and panels using CUF approach, differential geometry and differential quadrature method. *Composite Structures*, 107:675–697, 2014.

[31] A.J.M. Ferreira, E. Carrera, M. Cinefra, E. Viola, F. Tornabene, N. Fantuzzi, and A.M. Zenkour. Analysis of thick isotropic and cross-ply laminated plates by generalized differential quadrature method and a unified formulation. *Composites Part B: Engineering*, 58:544–552, 2014.

[32] S. Brischetto and E. Carrera. Thermal stress analysis by refined multilayered composite shell theories. *Journal of Thermal Stresses*, 32(1-2):165–186, 2008.

[33] M. D'Ottavio, D. Ballhause, B. Kröplin, and E. Carrera. Closed-form solutions for the free-vibration problem of multilayered piezoelectric shells. *Computers & Structures*, 84(22–23):1506–1518, 2006.

[34] M. D'Ottavio. A Sublaminate Generalized Unified Formulation for the analysis of composite structures. *Composite Structures*, 142:187–199, 2016.

[35] L. Demasi. ∞^3 hierarchy plate theories for thick and thin composite plates: the Generalized Unified Formulation. *Composite Structures*, 84(3):256–270, 2008.

[36] Y. Frostig, M. Baruch, O. Vilnay, and I. Sheinman. High-order theory for sandwich-beam behavior with transversely flexible core. *Journal of Engineering Mechanics*, 118(5):1026–1043, 1992.

[37] Y. Frostig and O.T. Thomsen. Non-linear thermo-mechanical behaviour of delaminated curved sandwich panels with a compliant core. *International Journal of Solids and Structures*, 48(14-15):2218–2237, 2011.

[38] M. D'Ottavio, L. Dozio, R. Vescovini, and O. Polit. Bending analysis of composite laminated and sandwich structures using sublaminate variable-kinematic Ritz models. *Composite Structures*, 155:45–62, 2016.

[39] R. Vescovini, M. D'Ottavio, L. Dozio, and O. Polit. Buckling and wrinkling of anisotropic sandwich plates. *International Journal of Engineering Science*, 130:136–156, 2018.

[40] R. Vescovini, M. D'Ottavio, L. Dozio, and O. Polit. Thermal buckling response of laminated and sandwich plates using refined 2-d models. *Composite Structures*, 176:313–328, 2017.

[41] R. Wijintjes, F. Simon, T. Haase, O. Unruh, and E. Tijs. Benchmark for experimentation of acoustic transmission loss applied to helicopter trim panels. In *42^{nd} European Rotorcraft Forum (ERF 2016)*, Lille, France, 5–8 September, 2016.

[42] J.N. Reddy. *Energy Principles and Variational Methods in Applied Mechanics.* John Wiley and Sons, New York, USA, 1984.

[43] R. Vescovini, L. Dozio, M. D'Ottavio, and O. Polit. On the application of the Ritz method to free vibration and buckling analysis of highly anisotropic plates. *Composite Structures*, 192:460–474, 2018.

[44] S. Brischetto. An exact 3D solution for free vibrations of multilayered cross-ply composite and sandwich plates and shells. *International Journal of Applied Mechanics*, 06(6):1–42, 2014.

[45] C.N. Phan, Y. Frostig, and G.A. Kardomateas. Analysis of sandwich beams with a compliant core and with in-plane rigidity-extended high-order sandwich panel theory versus elasticity. *Journal of Applied Mechanics*, 79(4):041001, 2012.

[46] M.Y. Yasin and S. Kapuria. An efficient layerwise finite element for shallow composite and sandwich shells. *Composite Structures*, 98:202–214, 2013.

[47] F. Simon. Proposal of reference panels (ST1.1). Internal report, Garteur AG20/ST1.1, April 2013.

Table 1: *Mechanical properties and densities of materials.*

Material	E_1 [GPa]	E_2 [GPa]	E_3 [GPa]	ν_{12}	ν_{13}	ν_{23}	G_{12} [GPa]	G_{13} [GPa]	G_{23} [GPa]	ρ [kg/m^3]
Skin-1	132.38	10.756	10.756	0.24	0.24	0.49	5.6537	5.6537	3.603	1600
Core-1	0.18	0.18	0.18	0.37	0.37	0.37	/	/	/	50
Skin-2	172.5	6.9	6.9	0.25	0.25	0.25	3.45	3.45	2.76	/
Core-2	0.276	0.276	3.45	0.25	0.02	0.02	0.1104	0.414	0.414	/

Table 2: *Non-dimensional circular frequencies* $\hat{\omega}_{m,n} = \dfrac{b^2}{h}\sqrt{\dfrac{\rho^{\text{face}}}{E_2^{\text{face}}}}\omega_{m,n}$ *for simply-supported sandwich deep shell* ($b/R = \pi/3$) *with laminate skins and different combinations of half-wave numbers* (25×25 *trial functions*).

Mode		$R/h = 1000$		$R/h = 100$		$R/h = 10$		$R/h = 5$	
(m,n)		3D [44]	S-GUF	3D [44]	S-GUF	3D [44]	S-GUF	3D [44]	S-GUF
(1,1)	I	338.13	338.14	35.247	35.248	5.4162	5.4165	2.9011	2.9014
	II	4875.2	4875.8	487.52	487.58	48.665	48.674	18.627	18.628
	III	8781.1	8782.0	877.98	878.08	61.782	61.791	24.208	24.217
(1,2)	I	143.15	143.16	42.140	42.144	9.9226	9.9236	5.6055	5.6087
	II	6334.6	6335.0	633.45	633.50	63.059	63.066	18.218	18.219
	III	16759	16761	1675.2	1675.4	74.258	74.266	30.815	30.823
(2,1)	I	723.96	723.96	73.860	73.860	9.1701	9.1704	4.7742	4.7747
	II	8488.9	8491.0	848.83	849.04	73.279	73.285	18.752	18.752
	III	9419.3	9419.3	941.81	941.81	84.391	84.433	40.481	40.526
(2,2)	I	354.29	354.30	54.967	54.968	11.148	11.149	6.2612	6.2645
	II	9736.1	9737.3	973.56	973.68	76.774	76.775	18.147	18.163
	III	16924	16925	1691.7	1691.9	96.967	97.002	46.652	46.695

Table 3: *Displacement and stress components of simply-supported double-core shallow sandwich shell ($b/R = .5$) subjected to bi-sinusoidal pressure load. Comparison between various kinematic models (15×15 trial functions).*

a/b	b/h		Exact [46]	$\mathrm{LD}_{4,4,3}$	$\mathrm{ED}_{7,7,6}$	$\mathrm{LD}_{1,1,0}$	S-GUF
1	5	$\hat{u}_z$(a/2,b/2,0)	5.2824	5.2824	4.8408	5.3181	5.2812
		$\hat{\sigma}_x$(a/2,b/2,-h/2)	-2.0731	-2.0731	-2.0745	-2.0787	-2.0757
		10$\hat{\sigma}_y$(a/2,b/2,h/2)	1.5395	1.5395	1.4542	1.4497	1.5458
		$\hat{\tau}_{xy}$(0,0,h/2)	1.6409	1.6409	1.5769	1.6535	1.6406
		$\hat{\tau}_{yz}$(a/2,0,0)	0.2001	0.2001	0.2003	0.1997	0.2002
	10	$\hat{u}_z$(a/2,b/2,0)	2.5850	2.5850	2.4768	2.5889	2.5847
		$\hat{\sigma}_x$(a/2,b/2,-h/2)	-1.9675	-1.9675	-1.9801	-1.9672	-1.9688
		10$\hat{\sigma}_y$(a/2,b/2,h/2)	1.2612	1.2612	1.2116	1.2392	1.2643
		$\hat{\tau}_{xy}$(0,0,-h/2)	1.4885	1.4885	1.4597	1.4904	1.4884
		$\hat{\tau}_{yz}$(a/2,0,0)	0.2021	0.2021	0.2034	0.2021	0.2022
2	5	$\hat{u}_z$(a/2,b/2,0)	9.0416	9.0784	8.2804	9.1187	9.0767
		$\hat{\sigma}_x$(a/2,b/2,-h/2)	-3.7989	-3.7989	-3.7693	-3.8090	-3.8031
		10$\hat{\sigma}_y$(a/2,b/2,h/2)	1.3594	1.3594	1.2462	1.2670	1.3664
		$\hat{\tau}_{xy}$(0,0,-h/2)	1.6680	1.6680	1.5778	1.6729	1.6678
		$\hat{\tau}_{yz}$(a/2,0,0)	0.3348	0.3348	0.3327	0.3348	0.3350
	10	$\hat{u}_z$(a/2,b/2,0)	4.3974	4.3974	4.1943	4.4004	4.3970
		$\hat{\sigma}_x$(a/2,b/2,-h/2)	-3.5216	-3.5216	-3.5172	-3.5225	-3.5240
		10$\hat{\sigma}_y$(a/2,b/2,h/2)	0.9654	0.9654	0.9099	0.9415	0.9718
		$\hat{\tau}_{xy}$(0,0,-h/2)	1.2841	1.2841	1.2461	1.2846	1.2841
		$\hat{\tau}_{yz}$(a/2,0,0)	0.3294	0.3294	0.3293	0.3294	0.3295
			Theory-related DOFs:	124	23	25	34
			Maximum relative error:	0.4%	8.8%	6.8%	0.7%

Table 4: *Mechanical properties and stacking sequence of triple-core trim panel.*

Material	Layer no.	h [mm]	$E_1 = E_2$	E_3	ν	G_{12}	G_{23}	G_{13}	ρ
Glass fabric	1-4; 10-13	0.275	21 GPa	21 GPa	0.13	3 GPa	3 GPa	3 GPa	1600 kg/m^3
Nomex	5; 9	3.000	1 MPa	330 MPa	0	1 MPa	85 MPa	38 MPa	96 kg/m^3
Glue	6; 8	0.240	1.95 GPa	1.95 GPa	0.4	0.7 GPa	0.7 GPa	0.7 GPa	1050 kg/m^3
Melanine foam	7	13.00	0.5 MPa	0.23 MPa	0	95 kPa	95 kPa	95 kPa	11.7 kg/m^3

Table 5: *Fundamental frequencies (Hz) of fully clamped triple-core shell. Comparison between S-GUF and layer-wise models (*20×20 *trial functions).*

b/h	5		10		20		38.75		100	
b/R	S-GUF	$LD_{4,4,3}$	S-GUF	$LD_{4,4,3}$	S-GUF	$LD_{4,4,3}$	S-GUF	$LD_{4,4,3}$	S-GUF	$LD_{4,4,3}$
0	910.64	919.81	248.27	249.09	70.807	70.875	24.979	24.987	7.4872	7.4882
0.01	911.49	920.65	249.05	249.86	71.491	71.558	25.501	25.509	7.7580	7.7590
0.1	991.22	999.56	316.16	316.79	119.90	119.94	47.413	47.428	13.886	13.887
0.5	1845.4	1864.3	586.46	588.22	206.91	207.04	80.731	80.761	24.179	24.180
1	2033.0	2047.2	777.70	779.20	274.13	274.43	108.17	108.20	31.987	31.990
2	2538.5	2562.3	989.61	992.50	378.72	379.01	146.76	146.81	42.974	42.979

Table 6: *Strain and nondimensional stress components for clamped and simply-supported triple-core shells with* $a = b = 840$ *mm subjected to uniformly distributed pressure load. S-GUF model* $ED_{1,1,0}/\ LD_{1,1,0}/\ ED_{3,3,2}/\ LD_{1,1,0}/\ ED_{1,1,0}$ *and* 50×50 *trial functions.*

	CCCC						SSSS					
b/R	0	0.01	0.1	0.5	1	2	0	0.01	0.1	0.5	1	2
$\mu\varepsilon_z^{1,3}$	21.71	21.44	21.06	17.92	11.77	4.982	21.74	20.73	17.07	20.97	21.09	15.73
$\hat{\sigma}_x^{\text{top}}$	3858.	3878.	763.9	126.7	69.21	40.96	5421.	5993.	5333.	616.7	-185.3	-242.4
$\hat{\sigma}_x^{\text{bot}}$	-3858.	-3450.	71.33	79.45	26.67	4.163	-5421.	-4717.	652.2	691.5	-13.72	-291.3
$\hat{\sigma}_y^{\text{top}}$	3866.	5648.	4070.	887.4	546.6	337.6	5424.	5910.	4555.	242.8	-23.93	188.9
$\hat{\sigma}_y^{\text{bot}}$	-3866.	-1753.	2781.	617.1	211.3	44.76	-5424.	-4794.	561.8	1580.	896.0	186.8
$100\hat{\tau}_{xz}^{2,4}$	192.8	190.9	99.63	46.04	33.87	24.20	2004.	1992.	1189.	293.4	204.5	153.7
$100\hat{\tau}_{xz}^{1,2}$	156.9	154.8	63.80	12.49	4.148	.9671	1739.	1718.	886.7	48.65	.8566	4.729
$100\hat{\tau}_{yz}^{2,4}$	429.4	415.6	104.9	41.29	26.02	11.52	2030.	2020.	1401.	841.4	733.5	620.9
$100\hat{\tau}_{yz}^{1,2}$	349.8	333.7	21.85	-25.83	-18.12	-7.780	1740.	1722.	1078.	559.5	470.1	373.3

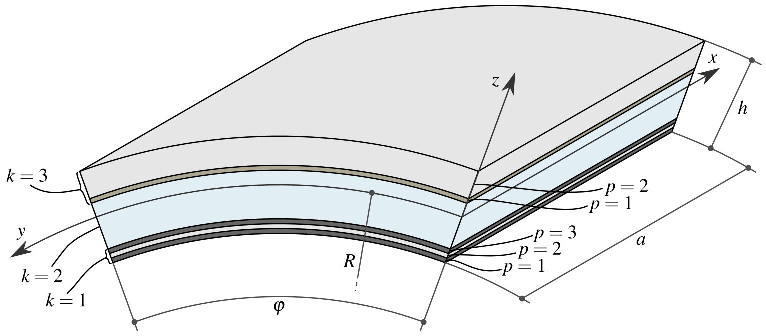

Figure 1: *Sketch of multilayered cylindrical shell.*

NEW FIGURE

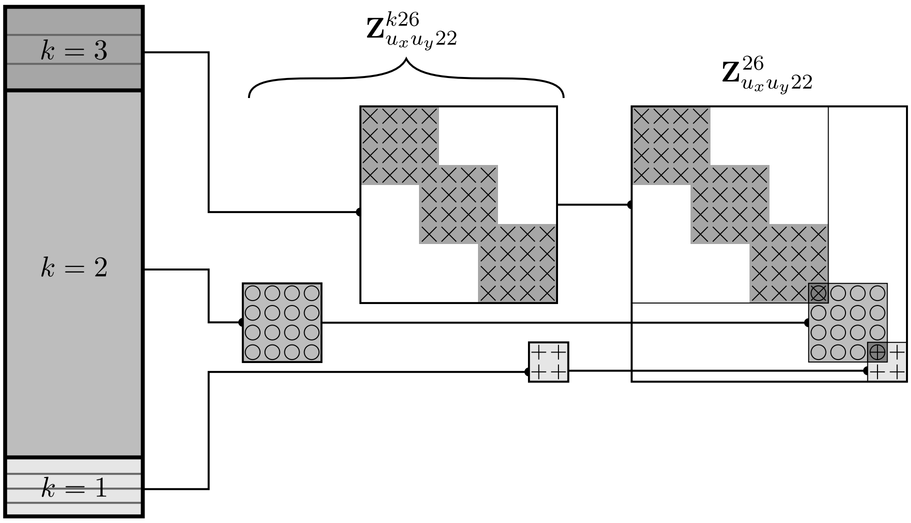

Figure 2: *Schematic representation of the assembly of thickness integrals. The kinematic model is* $LD_3/ED_3/ED_1$.

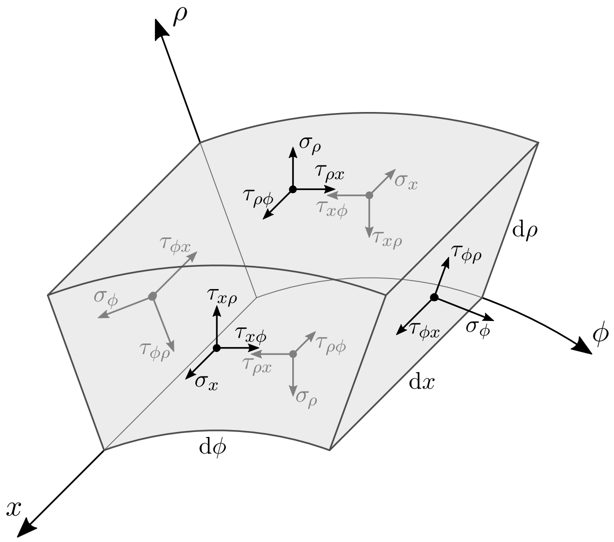

Figure 3: *Elementary volume in cylindrical coordinates.*

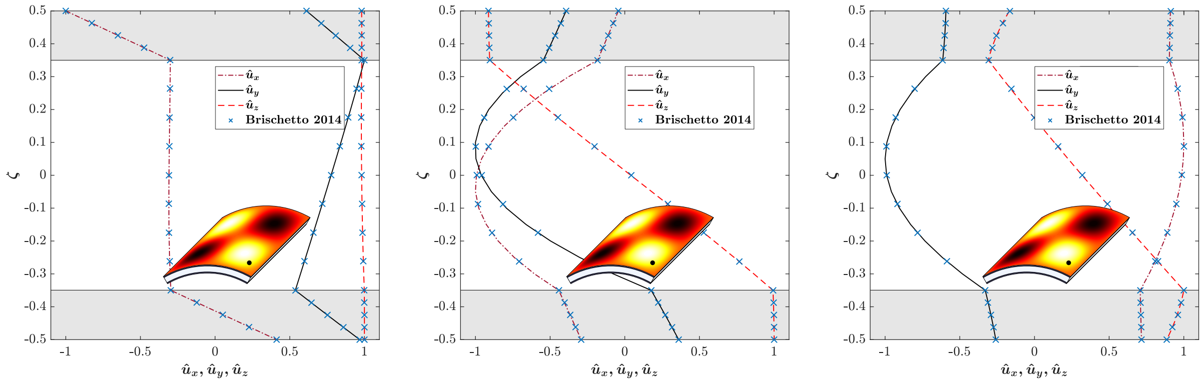

(a) (b) (c)

Figure 4: *Single-core shell with* $R/h = 10$ *– through-the-thickness non-dimensional displacements* $\hat{u}_i(a/8, b/8, \zeta)$ *for mode (2,2): (a) mode I, (b) mode II, (c) mode III.*

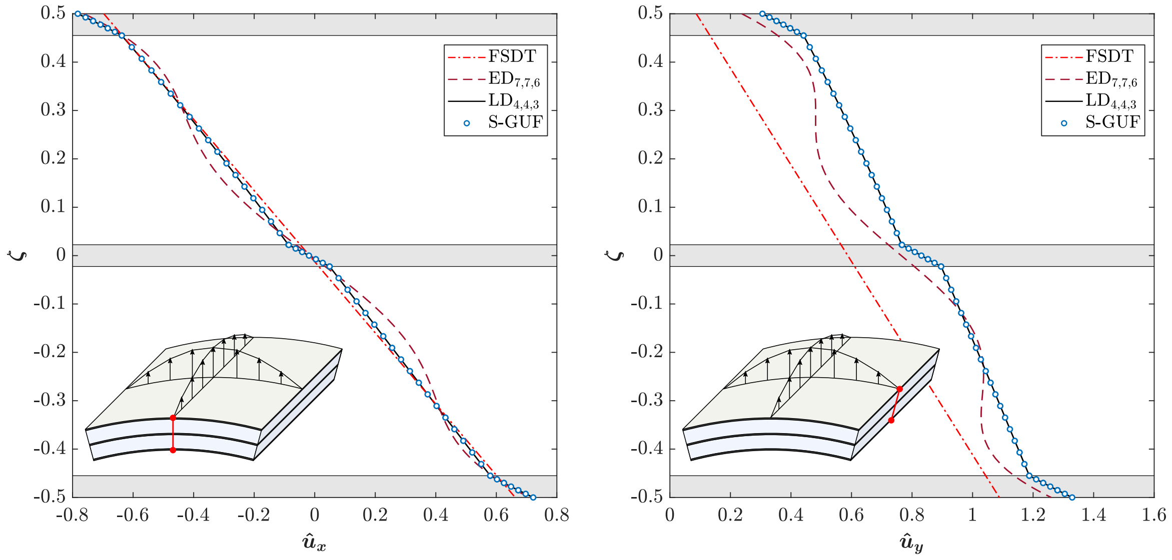

(a)

(b)

Figure 5: *Non-dimensional displacements versus non-dimensional thickness coordinate for square double-core shell: (a) $\hat{u}_x(0, b/2, \zeta)$, (b) $\hat{u}_y(a/2, 0, \zeta)$.*

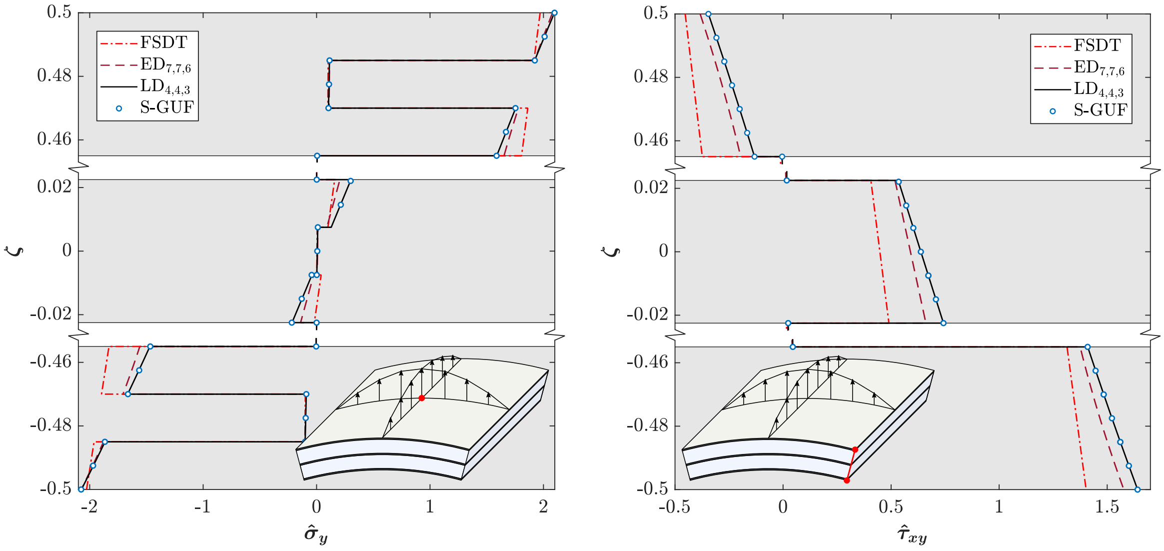

(a) (b)

Figure 6: *Non-dimensional in-plane stress components versus non-dimensional thickness coordinate for square double-core shell: (a)* $\hat{\sigma}_y(a/2, b/2, \zeta)$*, (b)* $\hat{\tau}_{xy}(0, 0, \zeta)$.

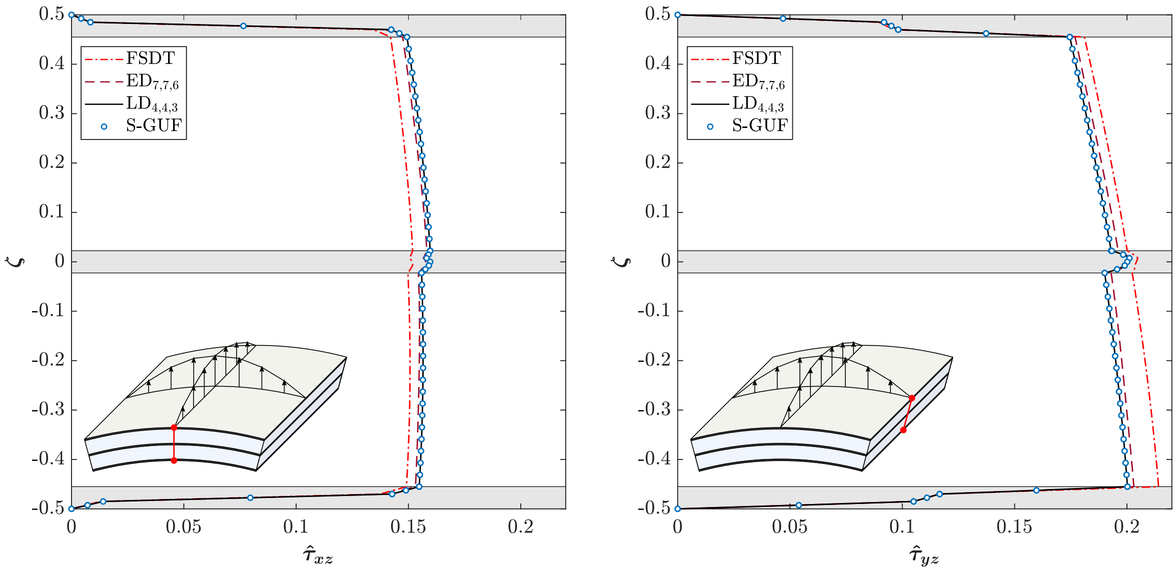

(a) (b)

Figure 7: *Non-dimensional transverse shear stress components versus non-dimensional thickness coordinate for square double-core shell: (a)* $\hat{\tau}_{xz}(0, b/2, \zeta)$*, (b)* $\hat{\tau}_{yz}(a/2, 0, \zeta)$.

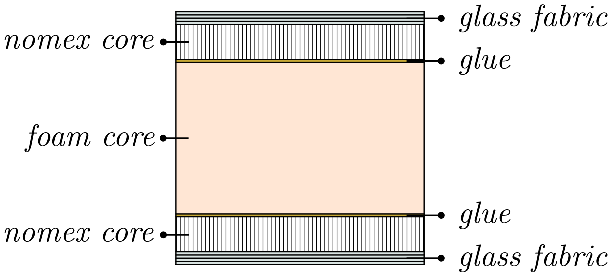

Figure 8: *Sketch of the stacking sequence of a triple-core sandwich panel.*

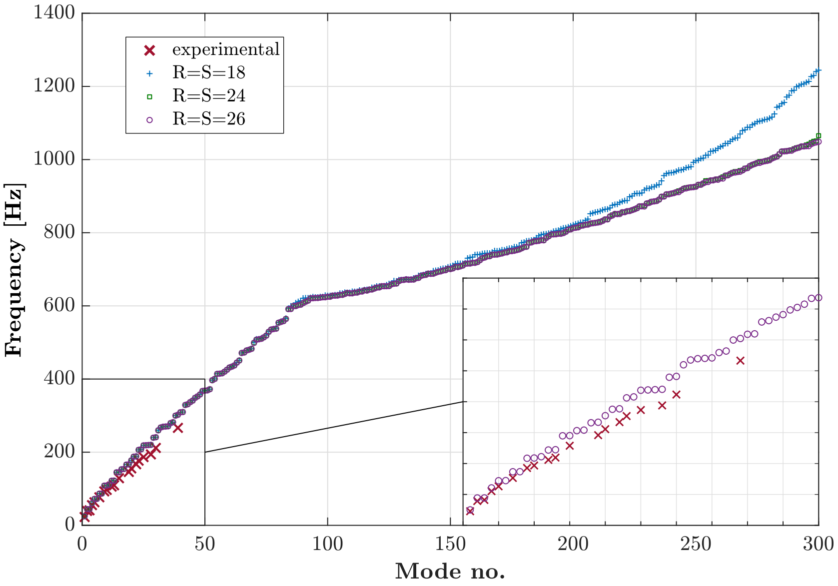

Figure 9: *Numerical/experimental comparison for natural frequencies of a flat triple-core sandwich panel.*

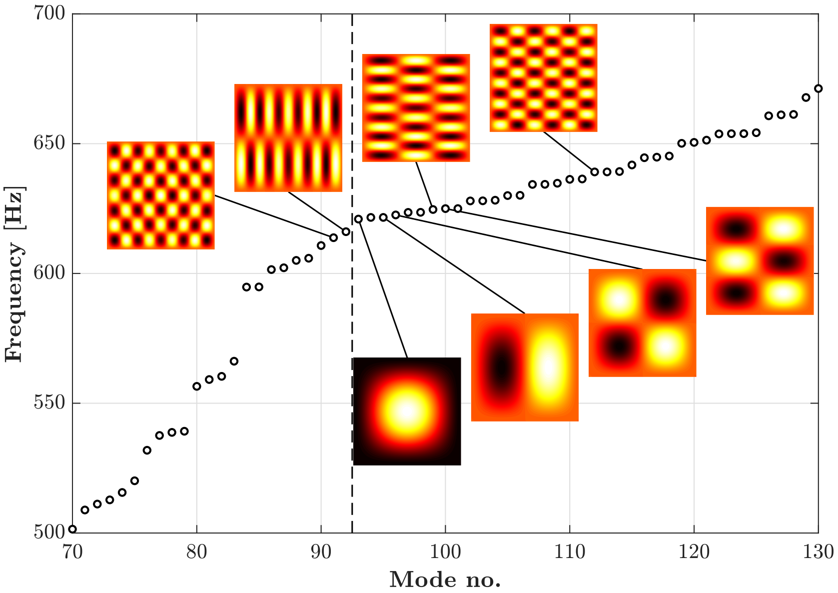

Figure 10: *Modal shapes in proximity of the change of slope: short half-wave modes without thickness extension (beyond the points), and long half-wave modes exhibiting thickness extension (below the points).*

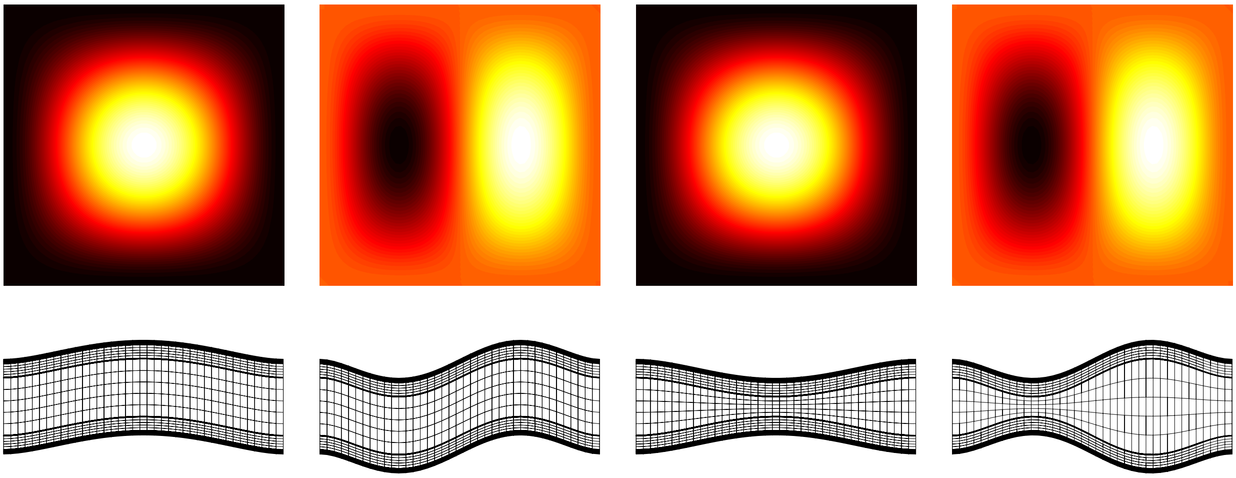

(a) Mode 1 @ 24.98 Hz (b) Mode 2 @ 44.29 Hz (c) Mode 93 @ 621.0 Hz (d) Mode 94 @ 621.7 Hz

Figure 11: *Modal shapes characterized by equal planar patterns, but different through-the-thickness behaviour.*

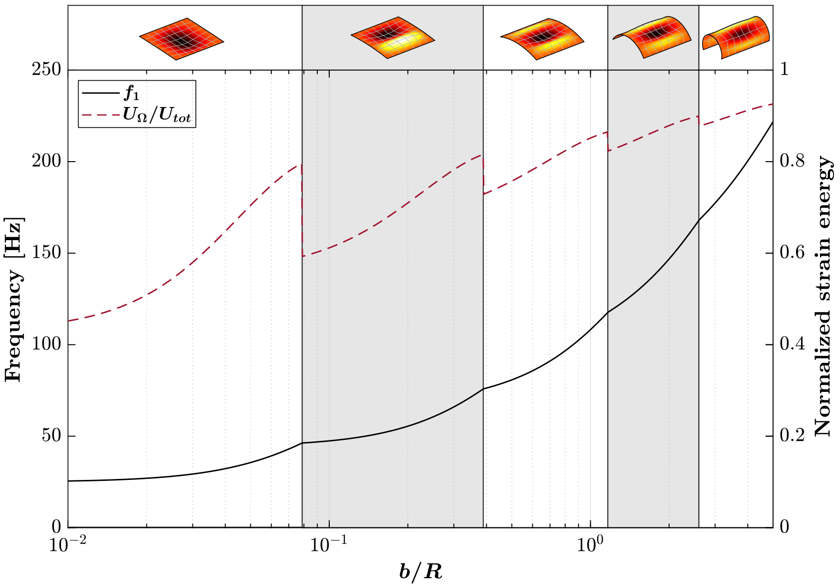

Figure 12: *Frequencies and modal shapes versus width-to-radius ratio (solid line) and relative in-plane strain energy contribution (dashed line). Simply-supported triple-core shell with dimension* 840×840 mm^2.

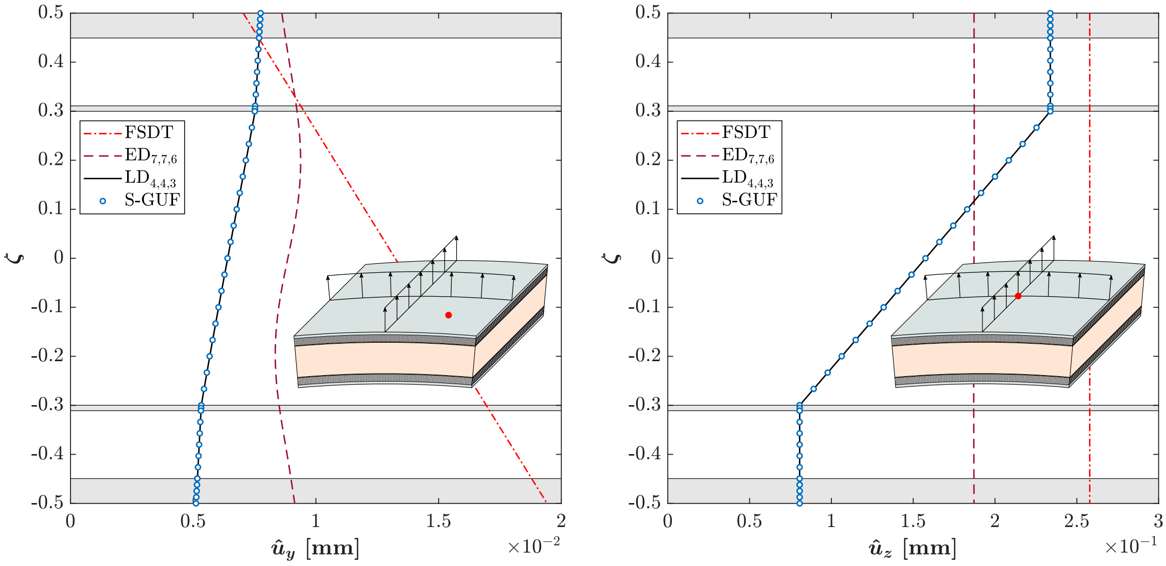

(a)

(b)

Figure 13: *Dimensional axial and radial displacement components in millimeters versus non-dimensional thickness coordinate for* $a = 840$ *mm,* $b = 420$ *mm and* $b/R = 1$*: (a)* $u_y(a/4, b/4)$*, (b)* $u_z(a/2, b/2)$*.*

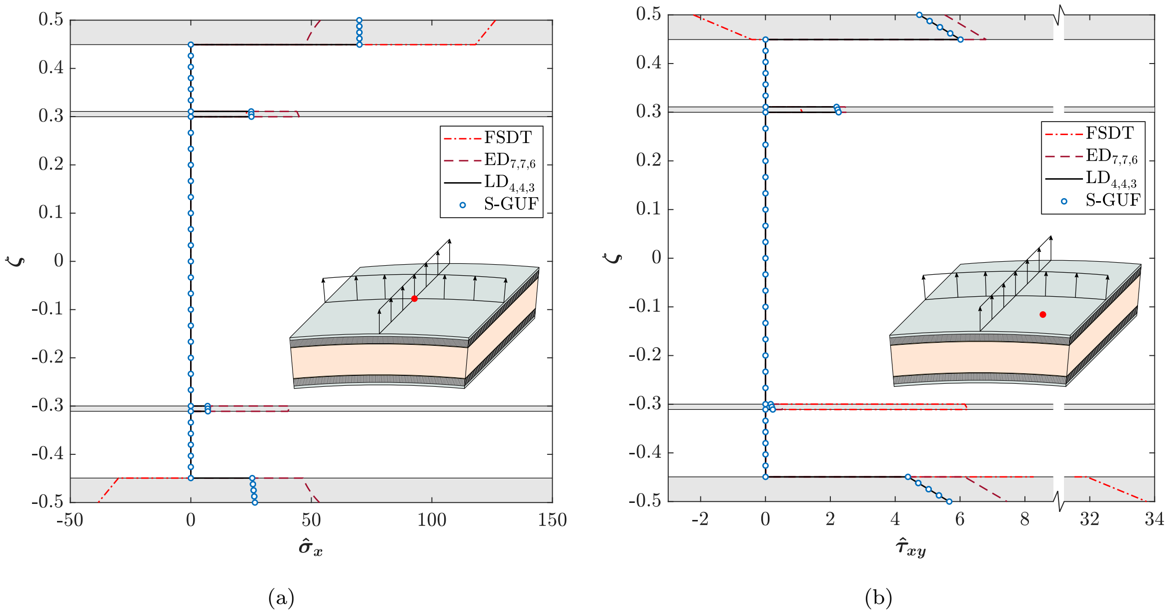

Figure 14: *Non-dimensional in-plane normal and shear stresses versus non-dimensional thickness coordinate for $a = b = 420$ mm and $b/R = 1$: (a) $\hat{\sigma}_x(a/2, b/2)$, (b) $\hat{\tau}_{xy}(a/4, b/4)$.*

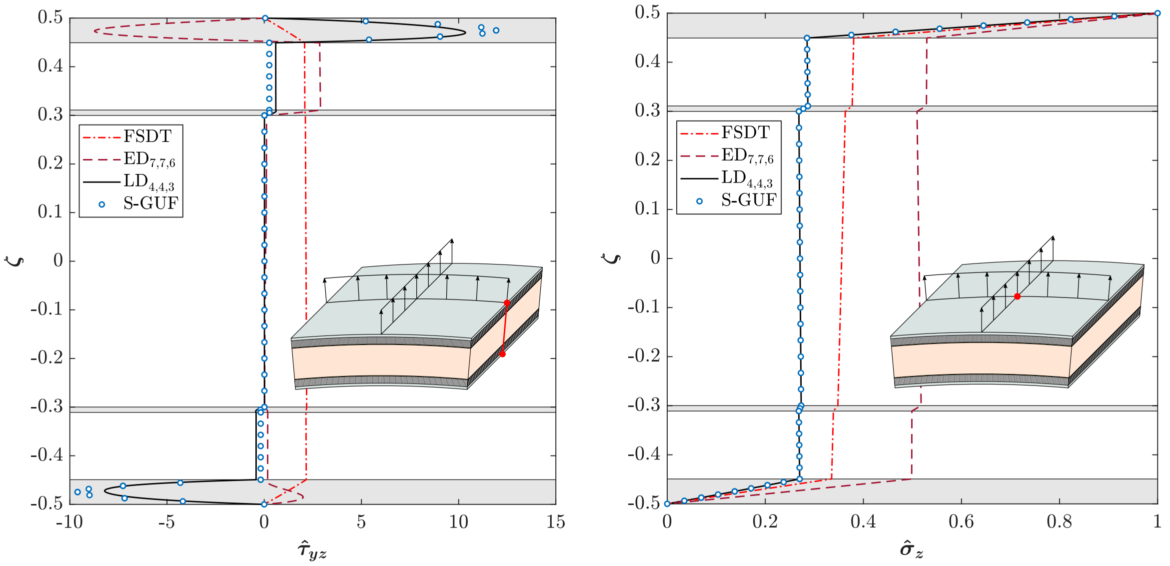

(a)

(b)

Figure 15: *Non-dimensional transverse shear and normal stresses versus non-dimensional thickness coordinate for* $a = 840$ *mm*, $b = 420$ *mm and* $b/R = 1$*: (a)* $\hat{\tau}_{yz}(a/2, 0)$*, (b)* $\hat{\sigma}_z(a/2, b/2)$.

5 Appendix

Ritz approximation of the Principle of Virtual Displacements

$$
\begin{aligned}
&\sum_{k=1}^{N_k}\sum_{p=1}^{N_p^k}\Big[\delta u^{p,k}_{x\alpha_{u_x}i}\rho^{p,k} Z^{p\alpha_{u_x}\beta_{u_x}}_{u_x u_x}\mathcal{I}^{0000}_{u_x u_x ij}\ddot{u}^{p,k}_{x\beta_{u_x}j} && + \delta u^{p,k}_{y\alpha_{u_y}i}\rho^{p,k} Z^{p\alpha_{u_y}\beta_{u_y}}_{u_y u_y}\mathcal{I}^{0000}_{u_y u_y ij}\ddot{u}^{p,k}_{y\beta_{u_y}j} \\
&\qquad + \delta u^{p,k}_{z\alpha_{u_z}i}\rho^{p,k} Z^{p\alpha_{u_z}\beta_{u_z}}_{u_z u_z}\mathcal{I}^{0000}_{u_z u_z ij}\ddot{u}^{p,k}_{z\beta_{u_z}j}\Big] + \\
&\sum_{k=1}^{N_k}\sum_{p=1}^{N_p^k}\Big[\delta u^{p,k}_{x\alpha_{u_x}i}\tilde{C}^{p,k}_{11} Z^{p\alpha_{u_x}\beta_{u_x}}_{u_x u_x 00}\mathcal{I}^{1010}_{u_x u_x ij}u^{p,k}_{x\beta_{u_x}j} && + \delta u^{p,k}_{x\alpha_{u_x}i}\tilde{C}^{p,k}_{12} Z^{p\alpha_{u_x}\beta_{u_y}}_{u_x u_y 11}\mathcal{I}^{1001}_{u_x u_y ij}u^{p,k}_{y\beta_{u_y}j} \\
&\qquad + \delta u^{p,k}_{x\alpha_{u_x}i}\tilde{C}^{p,k}_{12} Z^{p\alpha_{u_x}\beta_{u_z}}_{u_x u_z 10}\mathcal{I}^{1000}_{u_x u_z ij}u^{p,k}_{z\beta_{u_z}j} && + \delta u^{p,k}_{x\alpha_{u_x}i}\tilde{C}^{p,k}_{16} Z^{p\alpha_{u_x}\beta_{u_x}}_{u_x u_x 11}\mathcal{I}^{1001}_{u_x u_x ij}u^{p,k}_{x\beta_{u_x}j} \\
&\qquad + \delta u^{p,k}_{x\alpha_{u_x}i}\tilde{C}^{p,k}_{16} Z^{p\alpha_{u_x}\beta_{u_y}}_{u_x u_y 00}\mathcal{I}^{1010}_{u_x u_y ij}u^{p,k}_{y\beta_{u_y}j} && + \delta u^{p,k}_{x\alpha_{u_x}i}\tilde{C}^{p,k}_{13} Z^{p\alpha_{u_x}\beta_{u_z}}_{u_x \partial u_z 00}\mathcal{I}^{1000}_{u_x u_z ij}u^{p,k}_{z\beta_{u_z}j} \\
&\qquad + \delta u^{p,k}_{y\alpha_{u_y}i}\tilde{C}^{p,k}_{12} Z^{p\alpha_{u_y}\beta_{u_x}}_{u_y u_x 11}\mathcal{I}^{0110}_{u_y u_x ij}u^{p,k}_{x\beta_{u_x}j} && + \delta u^{p,k}_{y\alpha_{u_y}i}\tilde{C}^{p,k}_{22} Z^{p\alpha_{u_y}\beta_{u_y}}_{u_y u_y 22}\mathcal{I}^{0101}_{u_y u_y ij}u^{p,k}_{y\beta_{u_y}j} \\
&\qquad + \delta u^{p,k}_{y\alpha_{u_y}i}\tilde{C}^{p,k}_{22} Z^{p\alpha_{u_y}\beta_{u_z}}_{u_y u_z 21}\mathcal{I}^{0100}_{u_y u_z ij}u^{p,k}_{z\beta_{u_z}j} && + \delta u^{p,k}_{y\alpha_{u_y}i}\tilde{C}^{p,k}_{26} Z^{p\alpha_{u_y}\beta_{u_x}}_{u_y u_x 22}\mathcal{I}^{0101}_{u_y u_x ij}u^{p,k}_{x\beta_{u_x}j} \\
&\qquad + \delta u^{p,k}_{y\alpha_{u_y}i}\tilde{C}^{p,k}_{26} Z^{p\alpha_{u_y}\beta_{u_y}}_{u_y u_y 11}\mathcal{I}^{0110}_{u_y u_y ij}u^{p,k}_{y\beta_{u_y}j} && + \delta u^{p,k}_{y\alpha_{u_y}i}\tilde{C}^{p,k}_{23} Z^{p\alpha_{u_y}\beta_{u_z}}_{u_y \partial u_z 11}\mathcal{I}^{0100}_{u_y u_z ij}u^{p,k}_{z\beta_{u_z}j} \\
&\qquad + \delta u^{p,k}_{z\alpha_{u_z}i}\tilde{C}^{p,k}_{12} Z^{p\alpha_{u_z}\beta_{u_x}}_{u_z u_x 10}\mathcal{I}^{0010}_{u_z u_x ij}u^{p,k}_{x\beta_{u_x}j} && + \delta u^{p,k}_{z\alpha_{u_z}i}\tilde{C}^{p,k}_{22} Z^{p\alpha_{u_z}\beta_{u_y}}_{u_z u_y 21}\mathcal{I}^{0001}_{u_z u_y ij}u^{p,k}_{y\beta_{u_y}j} \\
&\qquad + \delta u^{p,k}_{z\alpha_{u_z}i}\tilde{C}^{p,k}_{22} Z^{p\alpha_{u_z}\beta_{u_z}}_{u_z u_z 20}\mathcal{I}^{0000}_{u_z u_z ij}u^{p,k}_{z\beta_{u_z}j} && + \delta u^{p,k}_{z\alpha_{u_z}i}\tilde{C}^{p,k}_{26} Z^{p\alpha_{u_z}\beta_{u_x}}_{u_z u_x 21}\mathcal{I}^{0001}_{u_z u_x ij}u^{p,k}_{x\beta_{u_x}j} \\
&\qquad + \delta u^{p,k}_{z\alpha_{u_z}i}\tilde{C}^{p,k}_{26} Z^{p\alpha_{u_z}\beta_{u_y}}_{u_z u_y 10}\mathcal{I}^{0010}_{u_z u_y ij}u^{p,k}_{y\beta_{u_y}j} && + \delta u^{p,k}_{z\alpha_{u_z}i}\tilde{C}^{p,k}_{23} Z^{p\alpha_{u_z}\beta_{u_z}}_{u_z \partial u_z 10}\mathcal{I}^{0000}_{u_z u_z ij}u^{p,k}_{z\beta_{u_z}j} \\
&\qquad + \delta u^{p,k}_{x\alpha_{u_x}i}\tilde{C}^{p,k}_{16} Z^{p\alpha_{u_x}\beta_{u_x}}_{u_x u_x 11}\mathcal{I}^{0110}_{u_x u_x ij}u^{p,k}_{x\beta_{u_x}j} && + \delta u^{p,k}_{x\alpha_{u_x}i}\tilde{C}^{p,k}_{26} Z^{p\alpha_{u_x}\beta_{u_y}}_{u_x u_y 22}\mathcal{I}^{0101}_{u_x u_y ij}u^{p,k}_{y\beta_{u_y}j} \\
&\qquad + \delta u^{p,k}_{x\alpha_{u_x}i}\tilde{C}^{p,k}_{26} Z^{p\alpha_{u_x}\beta_{u_z}}_{u_x u_z 21}\mathcal{I}^{0100}_{u_x u_z ij}u^{p,k}_{z\beta_{u_z}j} && + \delta u^{p,k}_{x\alpha_{u_x}i}\tilde{C}^{p,k}_{66} Z^{p\alpha_{u_x}\beta_{u_x}}_{u_x u_x 22}\mathcal{I}^{0101}_{u_x u_x ij}u^{p,k}_{x\beta_{u_x}j} \\
&\qquad + \delta u^{p,k}_{x\alpha_{u_x}i}\tilde{C}^{p,k}_{66} Z^{p\alpha_{u_x}\beta_{u_y}}_{u_x u_y 11}\mathcal{I}^{0110}_{u_x u_y ij}u^{p,k}_{y\beta_{u_y}j} && + \delta u^{p,k}_{x\alpha_{u_x}i}\tilde{C}^{p,k}_{36} Z^{p\alpha_{u_x}\beta_{u_z}}_{u_x \partial u_z 11}\mathcal{I}^{0100}_{u_x u_z ij}u^{p,k}_{z\beta_{u_z}j} \\
&\qquad + \delta u^{p,k}_{y\alpha_{u_y}i}\tilde{C}^{p,k}_{16} Z^{p\alpha_{u_y}\beta_{u_x}}_{u_y u_x 00}\mathcal{I}^{1010}_{u_y u_x ij}u^{p,k}_{x\beta_{u_x}j} && + \delta u^{p,k}_{y\alpha_{u_y}i}\tilde{C}^{p,k}_{26} Z^{p\alpha_{u_y}\beta_{u_y}}_{u_y u_y 11}\mathcal{I}^{1001}_{u_y u_y ij}u^{p,k}_{y\beta_{u_y}j} \\
&\qquad + \delta u^{p,k}_{y\alpha_{u_y}i}\tilde{C}^{p,k}_{26} Z^{p\alpha_{u_y}\beta_{u_z}}_{u_y u_z 10}\mathcal{I}^{1000}_{u_y u_z ij}u^{p,k}_{z\beta_{u_z}j} && + \delta u^{p,k}_{y\alpha_{u_y}i}\tilde{C}^{p,k}_{66} Z^{p\alpha_{u_y}\beta_{u_x}}_{u_y u_x 11}\mathcal{I}^{1001}_{u_y u_x ij}u^{p,k}_{x\beta_{u_x}j} \\
&\qquad + \delta u^{p,k}_{y\alpha_{u_y}i}\tilde{C}^{p,k}_{66} Z^{p\alpha_{u_y}\beta_{u_y}}_{u_y u_y 00}\mathcal{I}^{1010}_{u_y u_y ij}u^{p,k}_{y\beta_{u_y}j} && + \delta u^{p,k}_{y\alpha_{u_y}i}\tilde{C}^{p,k}_{36} Z^{p\alpha_{u_y}\beta_{u_z}}_{u_y \partial u_z 00}\mathcal{I}^{1000}_{u_y u_z ij}u^{p,k}_{z\beta_{u_z}j} \\
&\qquad + \delta u^{p,k}_{y\alpha_{u_y}i}\tilde{C}^{p,k}_{44} Z^{p\alpha_{u_y}\beta_{u_y}}_{u_y u_y 20}\mathcal{I}^{0000}_{u_y u_y ij}u^{p,k}_{y\beta_{u_y}j} && - \delta u^{p,k}_{y\alpha_{u_y}i}\tilde{C}^{p,k}_{44} Z^{p\alpha_{u_y}\beta_{u_y}}_{u_y \partial u_y 10}\mathcal{I}^{0000}_{u_y u_y ij}u^{p,k}_{y\beta_{u_y}j} \\
&\qquad - \delta u^{p,k}_{y\alpha_{u_y}i}\tilde{C}^{p,k}_{44} Z^{p\alpha_{u_y}\beta_{u_z}}_{u_y u_z 21}\mathcal{I}^{0001}_{u_y u_z ij}u^{p,k}_{z\beta_{u_z}j} && - \delta u^{p,k}_{y\alpha_{u_y}i}\tilde{C}^{p,k}_{45} Z^{p\alpha_{u_y}\beta_{u_x}}_{u_y \partial u_x 10}\mathcal{I}^{0000}_{u_y u_x ij}u^{p,k}_{x\beta_{u_x}j} \\
&\qquad - \delta u^{p,k}_{y\alpha_{u_y}i}\tilde{C}^{p,k}_{45} Z^{p\alpha_{u_y}\beta_{u_z}}_{u_y u_z 10}\mathcal{I}^{0010}_{u_y u_z ij}u^{p,k}_{z\beta_{u_z}j} && - \delta u^{p,k}_{y\alpha_{u_y}i}\tilde{C}^{p,k}_{44} Z^{p\alpha_{u_y}\beta_{u_y}}_{\partial u_y u_y 10}\mathcal{I}^{0000}_{u_y u_y ij}u^{p,k}_{y\beta_{u_y}j} \\
&\qquad + \delta u^{p,k}_{y\alpha_{u_y}i}\tilde{C}^{p,k}_{44} Z^{p\alpha_{u_y}\beta_{u_y}}_{\partial u_y \partial u_y 00}\mathcal{I}^{0000}_{u_y u_y ij}u^{p,k}_{y\beta_{u_y}j} && + \delta u^{p,k}_{y\alpha_{u_y}i}\tilde{C}^{p,k}_{44} Z^{p\alpha_{u_y}\beta_{u_z}}_{\partial u_y u_z 11}\mathcal{I}^{0001}_{u_y u_z ij}u^{p,k}_{z\beta_{u_z}j} \\
&\qquad + \delta u^{p,k}_{y\alpha_{u_y}i}\tilde{C}^{p,k}_{45} Z^{p\alpha_{u_y}\beta_{u_x}}_{\partial u_y \partial u_x 00}\mathcal{I}^{0000}_{u_y u_x ij}u^{p,k}_{x\beta_{u_x}j} && + \delta u^{p,k}_{y\alpha_{u_y}i}\tilde{C}^{p,k}_{45} Z^{p\alpha_{u_y}\beta_{u_z}}_{\partial u_y u_z 00}\mathcal{I}^{0010}_{u_y u_z ij}u^{p,k}_{z\beta_{u_z}j} \\
&\qquad - \delta u^{p,k}_{z\alpha_{u_z}i}\tilde{C}^{p,k}_{44} Z^{p\alpha_{u_z}\beta_{u_y}}_{u_z u_y 21}\mathcal{I}^{0100}_{u_z u_y ij}u^{p,k}_{y\beta_{u_y}j} && + \delta u^{p,k}_{z\alpha_{u_z}i}\tilde{C}^{p,k}_{44} Z^{p\alpha_{u_z}\beta_{u_y}}_{u_z \partial u_y 11}\mathcal{I}^{0100}_{u_z u_y ij}u^{p,k}_{y\beta_{u_y}j} \\
&\qquad + \delta u^{p,k}_{z\alpha_{u_z}i}\tilde{C}^{p,k}_{44} Z^{p\alpha_{u_z}\beta_{u_z}}_{u_z u_z 22}\mathcal{I}^{0101}_{u_z u_z ij}u^{p,k}_{z\beta_{u_z}j} && + \delta u^{p,k}_{z\alpha_{u_z}i}\tilde{C}^{p,k}_{45} Z^{p\alpha_{u_z}\beta_{u_x}}_{u_z \partial u_x 11}\mathcal{I}^{0100}_{u_z u_x ij}u^{p,k}_{x\beta_{u_x}j}
\end{aligned}
$$

$$
\begin{aligned}
&+ \delta u^{p,k}_{z\alpha_{u_z}i}\tilde{C}^{p,k}_{45}Z^{p\alpha_{u_z}\beta_{u_z}}_{u_z u_z 11}\mathcal{I}^{0110}_{u_z u_z ij}u^{p,k}_{z\beta_{u_z}j} && - \delta u^{p,k}_{x\alpha_{u_x}i}\tilde{C}^{p,k}_{45}Z^{p\alpha_{u_x}\beta_{u_y}}_{\partial u_x u_y 10}\mathcal{I}^{0000}_{u_x u_y ij}u^{p,k}_{y\beta_{u_y}j} \\
&+ \delta u^{p,k}_{x\alpha_{u_x}i}\tilde{C}^{p,k}_{45}Z^{p\alpha_{u_x}\beta_{u_y}}_{\partial u_x \partial u_y 00}\mathcal{I}^{0000}_{u_x u_y ij}u^{p,k}_{y\beta_{u_y}j} && + \delta u^{p,k}_{x\alpha_{u_x}i}\tilde{C}^{p,k}_{45}Z^{p\alpha_{u_x}\beta_{u_z}}_{\partial u_x u_z 11}\mathcal{I}^{0001}_{u_x u_z ij}u^{p,k}_{z\beta_{u_z}j} \\
&+ \delta u^{p,k}_{x\alpha_{u_x}i}\tilde{C}^{p,k}_{55}Z^{p\alpha_{u_x}\beta_{u_x}}_{\partial u_x \partial u_x 00}\mathcal{I}^{0000}_{u_x u_x ij}u^{p,k}_{x\beta_{u_x}j} && + \delta u^{p,k}_{x\alpha_{u_x}i}\tilde{C}^{p,k}_{55}Z^{p\alpha_{u_x}\beta_{u_z}}_{\partial u_x u_z 00}\mathcal{I}^{0010}_{u_x u_z ij}u^{p,k}_{z\beta_{u_z}j} \\
&- \delta u^{p,k}_{z\alpha_{u_z}i}\tilde{C}^{p,k}_{45}Z^{p\alpha_{u_z}\beta_{u_y}}_{u_z u_y 10}\mathcal{I}^{1000}_{u_z u_y ij}u^{p,k}_{y\beta_{u_y}j} && + \delta u^{p,k}_{z\alpha_{u_z}i}\tilde{C}^{p,k}_{45}Z^{p\alpha_{u_z}\beta_{u_y}}_{u_z \partial u_y 00}\mathcal{I}^{1000}_{u_z u_y ij}u^{p,k}_{y\beta_{u_y}j} \\
&+ \delta u^{p,k}_{z\alpha_{u_z}i}\tilde{C}^{p,k}_{45}Z^{p\alpha_{u_z}\beta_{u_z}}_{u_z u_z 11}\mathcal{I}^{1001}_{u_z u_z ij}u^{p,k}_{z\beta_{u_z}j} && + \delta u^{p,k}_{z\alpha_{u_z}i}\tilde{C}^{p,k}_{55}Z^{p\alpha_{u_z}\beta_{u_x}}_{u_z \partial u_x 00}\mathcal{I}^{1000}_{u_z u_x ij}u^{p,k}_{x\beta_{u_x}j} \\
&+ \delta u^{p,k}_{z\alpha_{u_z}i}\tilde{C}^{p,k}_{55}Z^{p\alpha_{u_z}\beta_{u_z}}_{u_z u_z 00}\mathcal{I}^{1010}_{u_z u_z ij}u^{p,k}_{z\beta_{u_z}j} && + \delta u^{p,k}_{z\alpha_{u_z}i}\tilde{C}^{p,k}_{13}Z^{p\alpha_{u_z}\beta_{u_x}}_{\partial u_z u_x 00}\mathcal{I}^{0010}_{u_z u_x ij}u^{p,k}_{x\beta_{u_x}j} \\
&+ \delta u^{p,k}_{z\alpha_{u_z}i}\tilde{C}^{p,k}_{23}Z^{p\alpha_{u_z}\beta_{u_y}}_{\partial u_z u_y 11}\mathcal{I}^{0001}_{u_z u_y ij}u^{p,k}_{y\beta_{u_y}j} && + \delta u^{p,k}_{z\alpha_{u_z}i}\tilde{C}^{p,k}_{23}Z^{p\alpha_{u_z}\beta_{u_z}}_{\partial u_z u_z 10}\mathcal{I}^{0000}_{u_z u_z ij}u^{p,k}_{z\beta_{u_z}j} \\
&+ \delta u^{p,k}_{z\alpha_{u_z}i}\tilde{C}^{p,k}_{36}Z^{p\alpha_{u_z}\beta_{u_y}}_{\partial u_z u_y 00}\mathcal{I}^{0010}_{u_z u_y ij}u^{p,k}_{y\beta_{u_y}j} && + \delta u^{p,k}_{z\alpha_{u_z}i}\tilde{C}^{p,k}_{36}Z^{p\alpha_{u_z}\beta_{u_x}}_{\partial u_z u_x 11}\mathcal{I}^{0001}_{u_z u_x ij}u^{p,k}_{x\beta_{u_x}j} \\
&+ \delta u^{p,k}_{z\alpha_{u_z}i}\tilde{C}^{p,k}_{33}Z^{p\alpha_{u_z}\beta_{u_z}}_{\partial u_z \partial u_z 00}\mathcal{I}^{0000}_{u_z u_z ij}u^{p,k}_{z\beta_{u_z}j}\Big] && = \delta u^{N^k_p,N_k}_{z0i}\mathcal{I}^{\mathrm{top}}_{u_z f_z i} + \delta u^{1,1}_{z1i}\mathcal{I}^{\mathrm{bot}}_{u_z f_z i}
\end{aligned}
\tag{45}
$$